SEISMIC STRUCTURE OF THE WESTERN U.S. MANTLE AND ITS RELATION TO REGIONAL TECTONIC AND MAGMATIC ACTIVITY

by

BRANDON SCHMANDT

A DISSERTATION

Presented to the Department of Geological Sciences
and the Graduate School of the University of Oregon
in partial fulfillment of the requirements
for the degree of
Doctor of Philosophy

September 2011

DISSERTATION APPROVAL PAGE

Student: Brandon Schmandt

Title: Seismic Structure of the Western U.S. Mantle and Its Relation to Regional Tectonic and Magmatic Activity

This dissertation has been accepted and approved in partial fulfillment of the requirements the Doctor of Philosophy degree in the Department of Geological Sciences by:

Eugene Humphreys	Chair
Douglas Toomey	Member
Emilie Hooft Toomey	Member
John Conery	Outside Member

and

Kimberly Andrews Epsy	Vice President for Research & Innovation/Dean of the Graduate School

Original approval signatures are on file with the University of Oregon Graduate School.

Degree awarded September 2011

DISSERTATION ABSTRACT

Brandon Schmandt

Doctor of Philosophy

Department of Geological Sciences

September 2011

Title: Seismic Structure of the Western U.S. Mantle and Its Relation to Regional Tectonic and Magmatic Activity

Approved: _____
Dr. Eugene Humphreys

Vigorous convective activity in the western U.S. mantle has long been inferred from the region's widespread intra-plate crustal deformation, volcanism, and high elevations, but the specific form of convective activity and the degree and nature of lithospheric involvement have been strongly debated. I design a seismic travel-time tomography method and implement it with seismic data from the EarthScope Transportable Array and complementary arrays to constrain three-dimensional seismic structure beneath the western U.S. Tomographic images of variations in compressional velocity, shear velocity, and the ratio of shear to compressional velocity in the western U.S. mantle to a depth of 1000 km are produced. Using these results I investigate mantle physical properties, Cenozoic subduction history, and the influence of small-scale lithospheric convection on regional tectonic and magmatic activity, with particular focus on southern California and the Pacific Northwest.

Chapter II presents a travel-time tomography method I designed and first implemented with data from southern California and the surrounding southwestern U.S.

The resulting images provide a new level of constraint on upper mantle seismic anomalies beneath the Transverse Ranges, southern Great Valley, Salton Trough, and southwestern Nevada volcanic field.

Chapter III presents tomographic images of the western U.S. mantle, identifies upper mantle volumes where partial melt is probable, and discusses implications of the apparently widespread occurrence of gravitational instabilities of continental lithsophere and the complex geometry and buoyancy of subducted ocean lithosphere imaged beneath the western U.S.

In Chapter IV, tomography images are used in conjunction with geologic constraints on major transitions in crustal deformation and magmatism to construct a model for Pacific Northwest evolution since the Cretaceous. Accretion in the Pacific Northwest at 55-50 Ma is suggested to stimulate roll-back of the flat subducting Farallon slab. This change in convergent margin structure is further suggested to drive the short-lived Challis magmatic trend and trigger the southward propagating Eocene-Oligocene transition from the Laramide orogeny to widespread crustal extension and ignimbrite magmatism.

This dissertation includes previously published co-authored material.

CURRICULUM VITAE

NAME OF AUTHOR: Brandon Schmandt

GRADUATE AND UNDERGRADUATE SCHOOLS ATTENDED:

University of Oregon, Eugene
University of Michigan, Ann Arbor
Warren Wilson College, Asheville, NC

DEGREES AWARDED:

Doctor of Philosophy, Geological Sciences, 2011, University of Oregon
Bachelor of Arts, Environmental Studies, 2006, Warren Wilson College

AREAS OF SPECIAL INTEREST:

Structure and dynamics of Earth's mantle
Tectonic evolution of the western U.S.

PROFESSIONAL EXPERIENCE:

GIS technician, Institute for Fisheries Research, University of Michigan, Ann Arbor, 2006-2007

Teaching Assistant, Department of Geological Sciences, University of Oregon, Eugene, 2007-2008

Research Assistant, Department of Geological Sciences, University of Oreogn, 2008-2011

GRANTS, AWARDS, AND HONORS:

Best Student Presentation, Seismological Society of America Annual Meeting, 4/2010

Invited talk: Seismological Society of America Annual Meeting, 4/2010
Invited talk: American Geophysical Union Fall Meeting, 12/2010
Invited talk: New Mexico Geologic Society Annual Meeting, 4/2011
Invited talk: EarthScope National Meeting, 5/2011

PUBLICATIONS:

Schmandt, B., K.G. Dueker, S.M. Hansen, J.J. Jasbinsek, Z. Zhang, (2011) A sporadic low-velocity layer atop the western U.S. mantle transition zone and short-wavelength variations in transition zone discontinuities, Geochemistry Geophysics Geosystems, doi:10.1029/2011GC003668, in press.

Levander, A., B. Schmandt, M. S. Miller, K. Liu, K. E. Karlstrom, R. S. Crow, C.-T. A. Lee, and E. D. Humphreys (2011) Ongoing Colorado Plateau uplift by delamination-style convective lithospheric downwelling, Nature, 472, 461–465, doi:10.1038/nature10001.

Schmandt, B. and Humphreys, E.D. (2011) Seismically Imaged Relict Slab from the 55 Ma Siletzia Accretion to Northwest USA, Geology, v. 39; no. 2; p. 175–178; doi: 10.1130/G31558.1

Crow, R.S., K.E., Karlstrom, Y. Asmerom, B. Schmandt, V. Polyak, S.A. DuFrane (2011) Shrinking of the Colorado Plateau via lithospheric mantle erosion: evidence from Nd and Sr isotopes and geochronology of Neogene basalts, Geology, v. 39; no. 1; p. 27–30; doi: 10.1130/G31611.1

Bezada, M. J., A. Levander, and B. Schmandt (2010) Subduction in the Southern Caribbean: Images from finite-frequency P-wave tomography, Journal of Geophysical Research, 115, B12333, doi:10.1029/2010JB007682.

Schmandt, B. and Humphreys, E.D. (2010) Complex subduction and small-scale convection revealed by body wave tomography of the western U.S. upper mantle, Earth and Planetary Science Letters, doi:10.1016/j.epsl.2010.06.047.

Schmandt, B. and Humphreys, E.D. (2010) Seismic heterogeneity and small-scale convection in the southern California upper mantle, Geochemistry Geophysics Geosystems. 11, Q05004, doi:10.1029/2010GC003042.

ACKNOWLEDGEMENTS

I have greatly benefitted from the academic support and genuine enthusiasm of my advisor, Gene Humphreys. Additionally, I thank Gene, Haiying Gao, Leland O'Driscoll, Max Bezada, and Stormy for sharing a constructive and enjoyable working environment.

TABLE OF CONTENTS

LIST OF FIGURES

Figure Page

CHAPTER I

INTRODUCTION

The seismic properties of the western U.S. mantle and the distribution of Cenozoic crustal deformation, magmatism, and uplift in the western U.S. Cordillera have long been recognized as globally anomalous. Reconstructing the evolution of subduction beneath the western margin of the North America plate, which has occurred continuously since the Jurassic, is central to understanding the origin of this anomalous continental upper mantle and intra-plate geologic activity.

During the middle to late Cretaceous a continuous North trending volcanic arc was active along the entire western plate margin indicating steep subduction of Farallon ocean lithosphere and creating a band of plutonic rocks visible at the surface today. At this time much of present-day Oregon and Washington had yet to be accreted to North America and the location of the Pacific Northwest portion of the volcanic arc was in western Idaho rather than in the location of the current Cascades arc. Late Cretaceous subsidence of the continental interior is evidenced by the marine sedimentary strata of the Cretaceous interior sea and indicates flattening of the subducting Farallon slab. Subsequent quiescence of the Cretaceous volcanic arc and propagation of magmatism and crustal shortening away from the plate margin and into the western U.S. interior are the key characteristics of the Laramide orogeny, which is thought to result from the Farallon slab subducting flat against the base of North America and closing off the asthenospheric wedge. After approximately 15-20 Myr of relatively sparse and low-productivity magmatism during the Laramide orogeny, widespread large-volume

ignimbrite magmatism occurred near the Cretaceous convergent margin in the Pacific Northwest, across the entire Basin and Range province, and in southwest Colorado. This activity is thought represent removal of the flat subducting Farallon slab, but explanations for fundamental aspects of this processes including its initiation, spatial and temporal progression, and lack of occurrence on the Colorado Plateau remain unconstrained. Prominent among the challenges in reconstructing Laramide and post-Laramide subduction history is that until recently seismologists have been unable to resolve the structure of nearly all the slab subducted during this time period.

Past seismological imaging of mantle structure clearly identified a coherent slab in the mid-mantle beneath eastern North America corresponding to subduction that occurred prior to the Laramide orogeny and also indentified slab subducted since the <10-15 Ma in the Pacific Northwest. However, robust identification of slab corresponding to Laramide and post-Laramide subduction remained elusive until the recent deployment of seismometers on a regular 70-km grid across the western U.S. (EarthScope's USArray). Herein, I present a new method for body-wave tomography that integrates complementary results from receiver function imaging of crustal thickness and dispersion of short-period Rayleigh waves, and I apply that method to the emerging USArray dataset and nearly all previously acquired western U.S. teleseismic data. The results provide a new level constraint on Laramide and post-Laramide subduction history including the implications of Eocene accretion of ocean lithsophere in the Pacific Northwest (PNW) and outward stepping of the PNW subduction zone to near its modern location. Additionally the tomography images reveal vigorous and widespread small-

scale convection in the western U.S. upper mantle and identify several regions of partially molten upper mantle.

Chapter II presents a new method for mantle tomography using multi-frequency travel-time residuals of teleseismic P-wave and S-wave data. Additionally, Chapter II presents the initial implementation of this method to a dataset in southern California and provides improved constraints on long-studied examples of small-scale lithospheric convection in the region.

Chapter III presents application of the tomography method to an unprecedented 2700 station dataset covering the entire western U.S. The images provide new insight into Laramide and post-Laramide subduction history, and identify widespread small-scale convection in the western U.S. upper mantle. Furthermore, the joint inversion of P and S data provides evidence for partial melt in the upper mantle beneath several active volcanic fields, and suggests melting occurs at depths which require the presence of significant volatile content in the nominally anhydrous minerals of that dominate the upper mantle assemblage.

Chapter IV presents a Cenozoic tectonic synthesis for the PNW that is constrained by regional magmatic history, a major transition in the mode of crustal deformation, and present-day geophysical structure of the PNW. I infer that Eocene accretion of ocean lithosphere in the Pacific Northwest stranded a segment of Farallon slab in the upper mantle roughly beneath the Cretaceous convergent margin, and that this event triggered an abrupt transition from Laramide contraction and magmatic quiescence to ignimbrite magmatism and post-Laramide extension including the formation of metamorphic core complexes.

I am the first author on three publications that constitute Chapters II, III, and IV. In each case I was responsible for data analysis and code-development, and the primary author of the manuscripts. All three publications were co-authored by my advisor Eugene Humphreys who supervised the seismological analyses, contributed to interpretation of the results, and assisted in editing of the manuscripts.

CHAPTER II

SEISMIC HETEROGENEITY AND SMALL-SCALE CONVECTION IN THE SOUTHERN CALIFORNIA UPPER MANTLE

This work was published in volume 11 of Geochemistry, Geophysics, Geosystems in May 2010. Coauthor Eugene Humphreys provided guidance in the analysis, interpretation, and editorial process. I performed all analysis and was the primary author of the manuscript.

1. Introduction

The structure of southern California lithosphere and underlying mantle are products of the complex evolution of the western North American plate boundary. More than 100 My of east-northeastward subduction (Engebretson et al., 1985), likely including low-angle subduction of a large buoyant ocean plateau ~80 Ma (Saleeby, 2003), was followed by passage of the northward migrating Mendocino triple junction (Atwater, 1970), which terminated subduction and initiated the San Andreas transform boundary that dissects and deforms the southern California landscape today (Fig. 2.1). Seismological studies show that the southern California upper mantle is, on average, anomalously slow, even with respect to the tectonically active western United States (Polet and Kanamori, 1997; Yang and Forsyth, 2006). Strong small-scale seismic heterogeneities within this slow mantle are widely interpreted as small-scale convection including downwelling of high-velocity lithospheric mantle related to oblique convergence in the Transverse Ranges (Humphreys et al., 1984; Bird and Rosenstock, 1984; Kohler 1999; Yang and Forsyth, 2006) and upwelling of asthenosphere associated

with oblique spreading in the Salton Trough (Raikes, 1980; Humphreys et al., 1984). Geodynamic modeling (Kosloff, 1977; Humphreys and Hager, 1990; Fay et al., 2008) suggests that stresses resulting from small-scale mantle convection contribute significantly to crustal deformation, but the geometry, magnitude and physical properties of heterogeneous mantle structures are too poorly resolved to rigorously test specific geodynamic hypotheses or discriminate among proposed tectonic origins. Progress in mantle imaging is an important step toward quantifying the role of small-scale convection in the active plate boundary deformation of southern California and better understanding the regional tectonic history.

In this paper we present new tomographic models of 3-D V_P, V_S, and V_P/V_S structure in the southern California mantle and discuss some implications of imaged structure for small-scale mantle convection and upper mantle physical state. Although there have been several efforts to image the southern California mantle with teleseismic body-waves (Hadley and Kanamori, 1977; Raikes, 1980; Humphreys and Clayton, 1990; Revenaugh, 1995; Kohler et al., 1999; Kohler et al., 2003; Tian et al., 2007) this is the first study to simultaneously image P- and S-velocity and to use the entire Southern California Seismic Network (SCSN) broadband and short-period arrays in conjunction with nearly all other regional experiments and the uniform wide-aperture coverage of the Transportable Array (TA) component of the USArray. The primary goal of this study is to improve resolution of the geometry, magnitude, and physical properties of previously imaged seismic anomalies interpreted to represent small-scale upper mantle convection. By imaging V_P, V_S, and V_P/V_S perturbations we aim to identify where properties other than temperature contribute strongly to seismic heterogeneity.

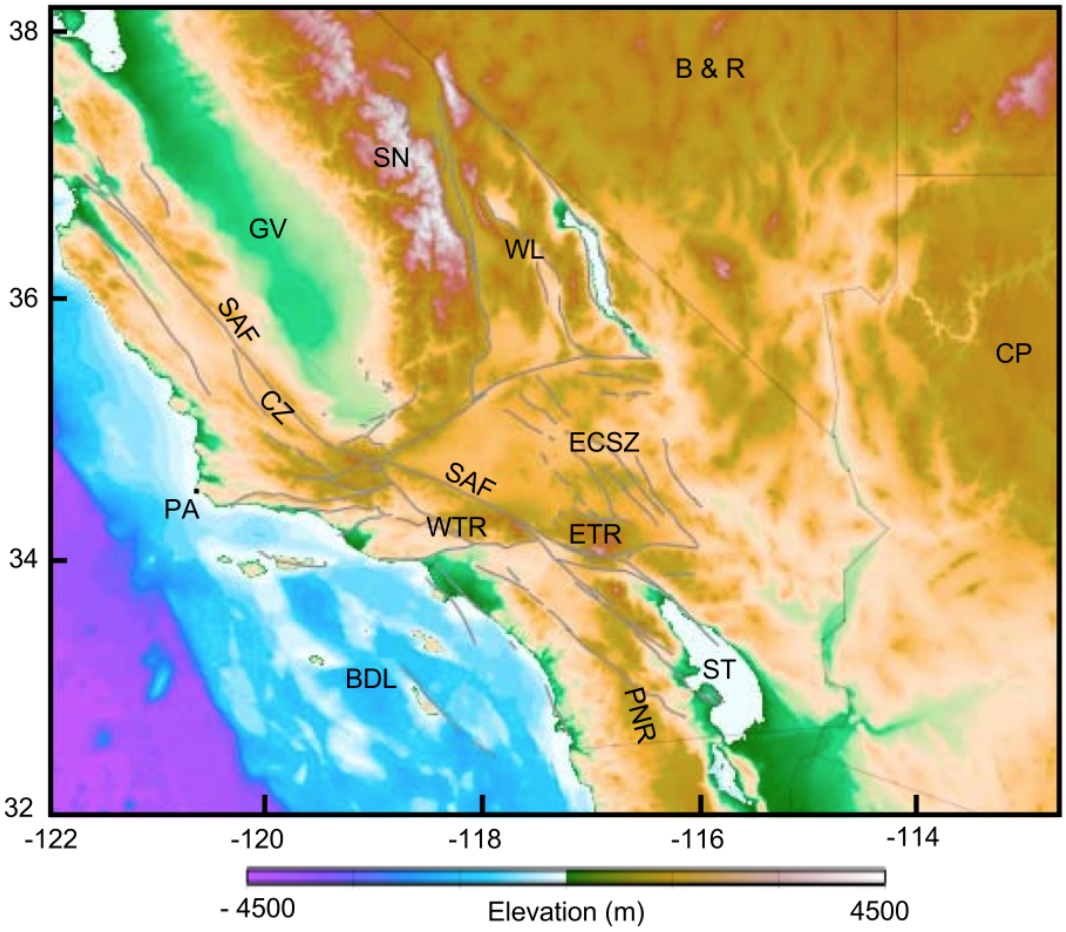

Figure 2.1. Topography of the southern California region. Geologic features: San Andreas Fault (SAF), Carrizo Plain (CZ), Point Arguello (PA), Borderland (BDL), Salton Trough (ST), Peninsular Ranges (PNR), western Transverse Ranges (WTR), eastern Transverse Ranges (ETR), eastern California shear zone (ECSZ), Walker Lane (WL), Sierra Nevada (SN), Great Valley (GV), Basin and Range (B&R), and Colorado Plateau (CP).

2. Relative travel-time data

2.1. Data

We use travel-time residuals of teleseismic P and S phases observed at 997 seismic stations (494 stations for S) in the southwestern U.S. to invert for 3-D perturbations in upper mantle V_P, V_S, and V_P/V_S (Fig. 2.2). Direct P (30-90°) and PKPdf phases observed on the vertical component are used for P-wave residuals. S-wave data are rotated to radial and tangential components and residuals are measured for direct S

(30-90°) phases observed on the tangential component. Relative residual times are measured by cross-correlation of band-pass-filtered waveforms (VanDecar and Crosson, 1990) in up to four Gaussian frequency bands with center frequencies of 1, 0.5, 0.3, 0.1 Hz for P-waves and 0.4, 0.1, 0.05 Hz for S-waves. Data from short-period stations are only used for 1 Hz P-wave residuals. In total, we use 92,927 P-wave residuals (45% 1 Hz, 29% 0.5 Hz, 22% 0.3 Hz, 4% 0.1 Hz) and 23,061 S-wave residuals (6% 0.4 Hz, 56% 0.1 Hz, 38% 0.05 Hz). We prefer to use more high-frequency data in the inversions because these data sample the mantle over smaller length-scales, there is dense station spacing in the region, and residual time uncertainty increases with period. However, relatively few high-quality S arrivals are observed at 0.4 Hz. The root mean square (RMS) values of P and S residuals are 0.37 s and 0.99 s, respectively. The RMS of the P residuals is within 0.36-0.38 for all frequency bands. The RMS of the S residuals decreases monotonically with decreasing frequency: 1.14 s for 0.4 Hz, 0.99 s for 0.1 Hz, and 0.96 s for 0.05 Hz. Ray path coverage throughout the southern California upper mantle is excellent as a result of the dense and long-running southern California and northern California Seismic Networks (NCSN), and several temporary deployments including the uniformly spaced wide-aperture stations of the TA. Use of stations up to several hundred km from southern California improves resolution of the deep upper mantle beneath southern California and minimizes edge effects in areas of interest. The main challenge in data coverage is the sudden geographic truncation of data at the Pacific Ocean and in Mexico (with relatively sparse station coverage in the southern California Borderland).

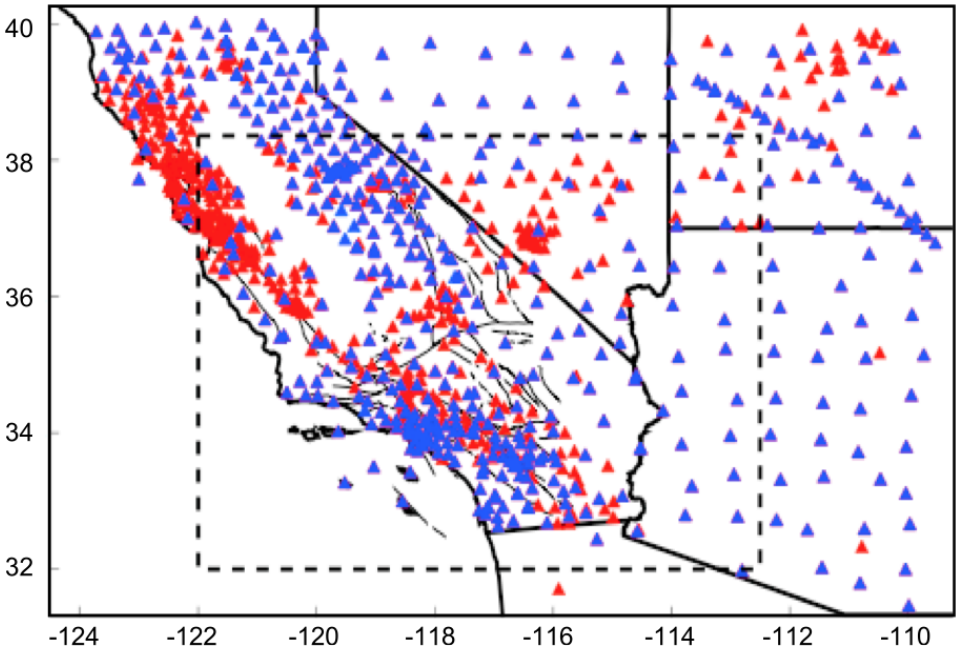

Figure 2.2. Station map. Blue triangles show stations that provided P and S data, and red triangles show stations that provided only P data (most of which are short-period instruments). Dashed line indicates the portion of the inversion shown in Figures 2.3–2.13; actual inversion includes entire map area at the surface, widening with depth.

We use topography and regional crustal velocity and thickness models to calculate travel-time corrections for crustal heterogeneity. Correction times are calculated by ray theory, and potential errors associated with frequency dependence (Ristema et al., 2009) are expected to be small for the phases and frequencies in our relative travel-time dataset. Recent results using data from the TA provide constraints on variations in crust velocity (Yang et al., 2008; Lin, et al., 2008) and thickness (Gilbert, in review) across the southwestern U.S. These results serve as a regional background model, which is replaced by higher-resolution local earthquake tomography studies that cover most of California. For southern California we use the adjoint tomography model of Tape et al. [2009], which has a Moho based on the results of Yan and Clayton [2007], and for central and northern California we use the crust tomography model of Thurber et al. [2009]. The

boundaries of the higher-resolution models are smoothly graded into the background regional model to avoid abrupt changes. In some areas only V_P or V_S models are available and it is necessary to scale V_S to V_P or vice-versa. In these cases, we use V_P/V_S of 1.78 for the crust, except in areas known to have thick sediment cover, such as in the Great Valley, where we use V_P/V_S of 1.9 in the upper 10 km. This simple scaling of V_S to V_P or V_P to V_S will introduce some error, but these errors are small compared to the errors that would be introduced by ignoring strong upper crustal structures such as basins and crystalline mountain ranges. The respective P and S crustal corrections have RMS values of 0.11 and 0.21 s, and the effects of reasonable variations in V_P/V_S would be a negligible $\sim$<20%. After correcting the travel-time residuals for crust structure, the RMS of the P and S residuals is 0.33 and 0.93, respectively, which is approximately the same RMS value as the raw residuals. This indicates that there is not a simple correlation between the crust corrections and raw travel-time residuals. The absence of correlation between crustal and mantle delays cautions against relying solely on inversion-based station terms to correct for the influence of the crust, because this procedure serves to reduce the magnitude of travel-time residuals and would therefore lead to a diminished recovery of the amplitude of mantle heterogeneity.

2.2. Regression analysis of P and S residuals

Linear regression of P and S travel-time residuals for common stations and events provides an estimate of ray path integrated $\delta ln V_S/\delta ln V_P$ in the region. Assuming that the differences between P and S ray paths and wavelengths have a small effect on the observed residuals, then $\delta t_S = a\delta t_P + b$ where a is a function of the path integrated velocity variations (Hales and Doyle, 1967),

$$a = (\delta V_S/\delta V_P)(V_P/V_S)^2. \quad (1)$$

Because we use relative delays times, the mean of all the residual times and the *b* value are equal to zero. We use ~10,000 P (0.5 Hz and 0.3 Hz) and S (0.1 Hz) residuals from events with at least 30 common stations to estimate the value of *a*. The linear fit with *a* = 2.86 minimizes a weighted sum of the squared errors and accounts for uncertainty in travel-time residuals estimated using the method of VanDecar and Crosson [1990] (Fig. 2.3). This *a* value corresponds to $\delta ln V_S/\delta ln V_P$ of 1.58 if we assume an average upper mantle V_P/V_S of 1.81 as in AK135 (Kennett and Engdahl, 1995). Mantle temperature variations are predicted to produce $\delta ln V_S/\delta ln V_P$ of ~1.2 – 2, (Kern and Richter, 1981; Anderson, 1992; Goes et al., 2000) depending on the assumed attenuation structure and mantle mineralogy, with the highest values corresponding to lower Q than is observed in the southern California mantle. To account for the anelastic contribution of temperature variations we use a mean Q_S in the upper 200 km of 95, as determined by Yang and Forsyth [2008], and we assume that the mantle is a Poisson solid with negligible bulk attenuation to calculate a mean Q_P in the upper 200 km of 214. Using these Q values with the temperature derivatives of Karato [1993], $\delta ln V_S/\delta ln V_P$ of ~1.65 is expected for thermal variations in the southern California upper mantle. Thus, it appears that the residual times are approximately consistent with temperature being the dominant cause of velocity variations. However, slope analysis of residual times is expected to underestimate *a,* and consequently $\delta ln V_S/\delta ln V_P$, because it is an integrated sampling of 3-D heterogeneity in the volume about the entire ray path. Furthermore, the wavelength of the measured S-waves is ~2 times the mean wavelength of the measured P-waves so

the S-wave residuals average over larger mantle volumes and likely underestimate the magnitude of V_S variations and hence $\delta ln V_S / \delta ln V_P$.

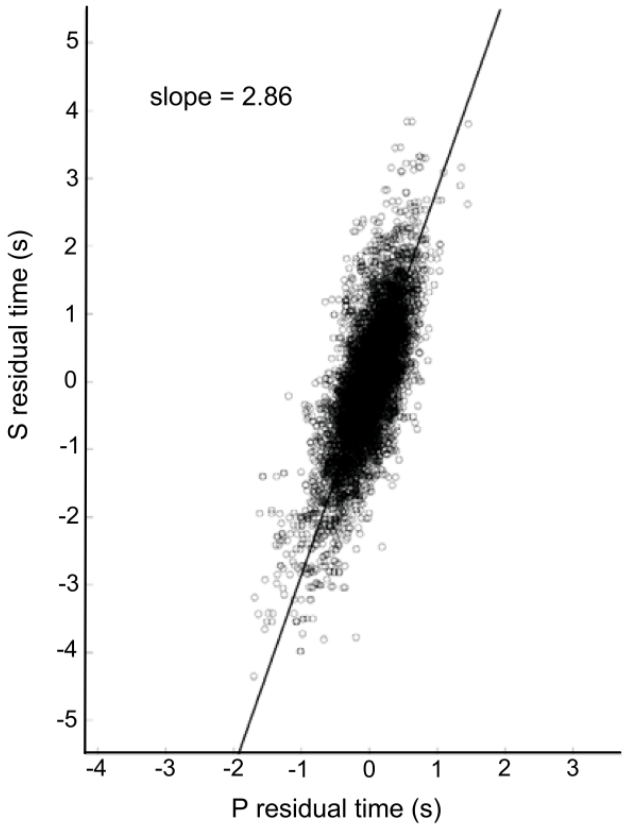

Figure 2.3. Regression analysis of P and S travel-time residuals. The best fit line has a slope of 2.86, which corresponds to $\delta ln V_S / \delta ln V_P$ of 1.58. Typical uncertainties for residual time measurements are about 1/20 of the dominant period. Using a bootstrap technique, the standard error for the slope a is 0.07, which corresponds to a standard error of 0.04 for $\delta ln V_S / \delta ln V_P$.

3. Tomographic inversion

We use frequency-dependent 3-D sensitivity kernels to relate travel-time residuals to perturbations of model parameters. We only consider sensitivity in the first Fresnel zone and we use an approximation of the Born theoretical, "banana-doughnut" kernel

(Dahlen et al., 2000; hereafter referred to as Born kernels) within the first Fresnel zone. Along a spectrum of complexity, our approach to calculating travel-time sensitivity lies somewhere between the "fat ray" approximation and the full Born kernel. We prefer a simplified form of the Born kernel for these reasons: (1) Sensitivity in the Born kernels varies on length-scales which are small compared to typical node spacing of 35-40 km (particularly in the outer Fresnel zones). Thus, the intricate structure will be under-sampled when the sensitivity values are integrated onto the model nodes. (2) Calculation of Born kernels requires knowledge of the shortest-time ray location in order to calculate how energy taking slightly different paths will affect the residual time as measured by cross-correlation. In reality, there is significant uncertainty in the location of the shortest time ray as a result of 3-D isotropic velocity variations and anisotropy. (3) Our approximate first Fresnel zone kernels are more computationally efficient and we think they achieve the main benefits of currently practical 3-D kernels for teleseismic tomography: an approximate means to interpret frequency dependence of travel-time residuals allowing better use of broadband data, and physically based smoothness criteria which reduce the need for regularization in the inversion.

The Born kernel formulation of Dahlen et al. [2000] is used to calculate the first Fresnel zone radius (R_{F1}) as a function of distance along the ray path (D_R). We calculate first Fresnel zone radii as a function of D_R for rays at 5 degree increments of epicentral distance, and repeat this step for each of the frequency bands in our dataset. We interpolate between these first Fresnel zone radii to determine R_{F1} for all rays in our dataset. We note that the relative amplitude of sensitivity in the Born kernel as a function of ray-normal distance (R_N) within any ray-normal plane is closely approximated by

$$K(R_N) \approx A \sin\left(\pi\left(\frac{R_N}{R_{F1}(D_R,\omega,\Delta)}\right)^2\right) \tag{2}$$

where A is a constant and R_{F1} is interpolated as a function of D_R, frequency band (ω), and epicentral distance (Δ). Equation 2 provides an approximation of the relative distribution of sensitivity within the first Fresnel zone. To determine the value of A, we use the fact that the integrated value of the full Born kernel in the volume about the ray is equal to the integrated value of ray-theoretical sensitivity along the ray length L

$$\int_V K(x)dV = \int_L \frac{1}{v(D_R)} dL \tag{3}$$

where K(x) is the 3-D Born sensitivity kernel and $v(D_R)$ is the reference velocity as a function of position along the ray. This is equivalent to the statement that the travel-time perturbation predicted by ray theory and Born theory is the same if the ray-normal width of the anomaly is greater than that of the Born kernel (Marquering et al., 1999; Hung et al., 2000). We use (2) and (3) to approximate sensitivity within the volume of the first Fresnel zone (K_{F1}) as

$$K_{F1}(R_N,D_R,\omega,\Delta) \approx \left[\frac{\int_L \frac{1}{v(D_R)} dL}{\int_{V_{F1}} \sin\left(\pi\left(\frac{R_N}{R_{F1}(D_R,\omega,\Delta)}\right)^2\right) dV_{F1}}\right] \sin\left(\pi\left(\frac{R_N}{F1_R(D_R,\omega,\Delta)}\right)^2\right) \tag{4}$$

where V_{F1} represents the entire volume of the first Fresnel zone about the ray length L. Finally, we apply ray-normal smoothing to the approximate first Fresnel zone kernels to address ray location uncertainty. The applied smoothing width increases with ray-path

distance from the station, increasing from 2 km at the Moho to 15 km at a distance of 700 km along the ray path (a typical ray length in our model domain). The smoothing width is selected based on the 3-D ray tracing tests of Saltzer and Humphreys [1997]. The resulting kernels are very similar to the Born kernels except that the integrated sensitivity is distributed only in the first Fresnel zone (Fig. 2.4).

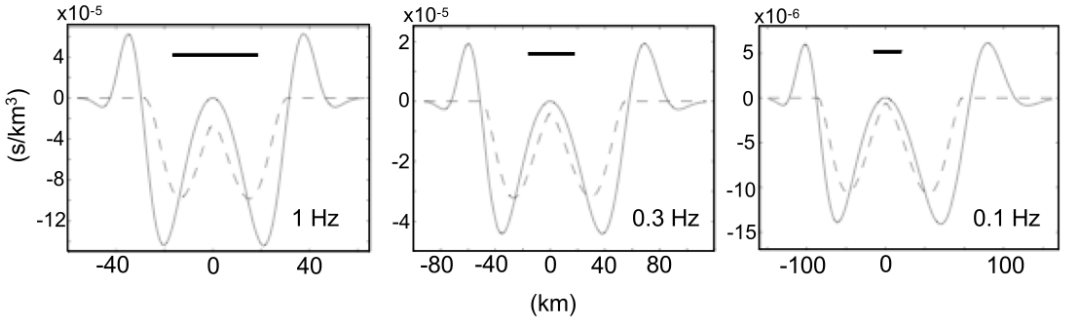

Figure 2.4. Travel-time sensitivity kernels. Comparison of our approximate first–Fresnel zone sensitivity kernels (dashed line) with "banana-doughnut" sensitivity kernels (solid line) of Dahlen et al. [2000]. The plots show ray-normal cross sections of sensitivity at a distance of 250 km from the receiver along the raypath for 1 Hz, 0.3 Hz, and 0.1 Hz P waves. The heavy black line shows the typical 35 km length scale of node spacing onto which kernel values are integrated.

Nodes at the vertices of an irregular, rectangular 3-D mesh parameterize the model space. The distance between vertical nodes increases gradually from 30 km (at 60-90 km depth) to 55 km (at >540 km depth) to address growing first Fresnel-zone width and decreasing resolution. Horizontal node spacing is smallest beneath the SCSN array footprint and gradually increases away from southern California with the largest spacing near and beyond the boundary of the entire array, where there is a paucity of crossing rays. Horizontal node spacing varies from 34 to 55 km in the shallow mantle and it dilates as a function of depth such that horizontal spacing varies from 45 to 70 km at a

depth of 650 km. The model domain extends from 35 km (top of the AK135 mantle) to 650 km depth. Resolution is poor in the 35 km layer as a result of near vertical ray path orientation, large variations in station density, variable crustal thickness and the fact that rays cluster at station locations. This layer tends to absorb both errors in the *a priori* crust model and crust and uppermost mantle velocity variations that are not well constrained by our data.

In addition to the V_P and V_S model parameters, we invert for station and event parameters. Because we correct for crust thickness and velocity variations, the station terms are only intended to address local site effects and errors in the *a priori* crust model; consequently, we apply strong station damping to keep the station terms from absorbing mantle structure. The RMS of the station terms is 0.06 s and 0.09 s for P and S, respectively. Event terms represent adjustment of the mean arrival time for the specific set of stations that record each event. These terms are important because we solve for velocity perturbations rather than absolute velocity, and the mean velocity structure varies significantly for different arrays in the southwestern U.S.

Gradient damping and norm damping are used to regularize the inverse problem. The geometry of the gradient damping is asymmetric such that the weight of the constraint is greatest in the plane normal to the mean ray path orientation as a function of depth. In the uppermost mantle, where teleseismic ray paths are nearly vertical, horizontal gradient damping receives 2.5 times the weight of vertical gradient damping. The relative horizontal/vertical weight decreases smoothly with depth to account for the increasing angle of inclination of teleseismic ray paths away from the receiver. At the 650-km base of the model, the horizontal-to-vertical ratio is ~1.3. Norm damping seeks

to find the smallest model that satisfies the travel-time data and most strongly penalizes perturbations that are weakly constrained by the data. Given the abundance and diversity of ray paths, we keep norm damping small so as to more accurately recover the amplitude of well-sampled anomalous structures while still providing a degree of penalty for strong perturbations in poorly sampled volumes.

We find an optimal solution to the regularized inverse problem by using the LSQR method (Paige and Saunders, 1982) to minimize the cost function

$$\mathbf{E} = ||A\mathbf{m} - \mathbf{d}||^2 + k_1||L\mathbf{m}||^2 + k_2||\mathbf{m}||^2. \quad (5)$$

Vector **m** contains the model parameters, and matrix A contains the partial derivatives that relate travel-time residuals to perturbations in model parameters; **d** are the data after crust corrections. The relative weights of the damping terms are given by k_1 and k_2. The L matrix represents the spatially varying smoothing constraint described above. We do this individually for the V_P and V_S models. The values of k_1 and k_2 for the P and S datasets are proportional to the magnitudes of the P and S data vectors.

We also construct a joint V_P and V_S model, which is found by simply summing the individual cost functions and adding additional regularization for $\delta ln V_S / \delta ln V_P$:

$$\mathbf{E}_{Vp/Vs} = \mathbf{E}_{Vp} + b^*\mathbf{E}_{Vs} + k_3||L_{Vp/Vs}\mathbf{m}_{\mathbf{P,S}}||^2 . \quad (6)$$

The scalar b is used to control the relative weight of the P and S datasets. In the model presented the P and S datasets are equally weighted by choosing the value of b such that $||\mathbf{d}_\mathbf{P}|| = b^*||\mathbf{d}_\mathbf{S}||$, b=1.52. Damping the gradient of $\delta ln V_S / \delta ln V_P$ variations regularizes the V_P/V_S model. Thus, we allow for significant departures from the reference V_P/V_S values

of AK135, but we impose simultaneous smoothness constraints on $\delta ln V_S$, $\delta ln V_P$, and $\delta ln V_S / \delta ln V_P$ structure. The resulting V_P/V_S model is calculated as

$$\delta ln(Vp/Vs) = [\ (\delta ln Vp \times Vp_0 + Vp_0)/(\ \delta ln Vs \times Vs_0 + Vs_0) - Vp_0/Vs_0\ ]\ /\ Vp_0/Vs_0, \qquad (7)$$

where Vp_0 and Vs_0 indicate the reference velocity values.

Details of the reference model only slightly influence of the location teleseismic ray paths in the upper mantle, and have insignificant influence on the magnitude of velocity variations. Our 1-D reference model uses TNA (Grand and Helmberger, 1984) for V_S above 410 km and AK135 (Kennett et al., 1995) at greater depth, and the V_P/V_S value from AK135 is used to calculate the reference V_P above 410 km. We use TNA rather than a southern California 1-D reference model because our inversion includes much of the southwestern U.S. and TNA is thought to better represent the average 1-D structure of this region.

Teleseismic phases often are observed to have a travel-time moveout that is slightly different from that predicted by our reference model, owing to hypocenter miss-location and heterogeneous structure within and beyond the volume of the model domain. To minimize the effects of out-of-box structure without significantly diminishing the travel-time signal of the in-box structure, we perform an initial inversion and then adjust the moveout of each event to minimize the misfit (in a least-squares sense) with respect to the initial 3-D model. The final inversion is performed with the adjusted ray parameters and travel-time residuals. The differences between the first and second inversions are generally small for the southwestern U.S., with 1-2% changes in variance reduction and only very minor changes to the 3-D model. (Optimization of event

moveout is a more important correction when large changes in lateral velocity occur on length-scales similar to the array aperture.)

Synthetic tests demonstrate expected model resolution with the assumptions of an isotropic elastic mantle, accurate ray locations, and banana-doughnut-like travel-time sensitivity. The synthetic structure consists of three checkerboard layers embedded in a neutral background (Fig. 2.5, 2.6), with each anomalous volume consisting of 8 nodes at the vertices of a ~35-50 km cube (size increases with depth in accord with node spacing). In general, the recovery of the input structure is excellent, although we find some streaking and amplitude loss of the input structures owing to the sub-vertical orientation of teleseismic rays and the preference for minimum energy structure in the inversion algorithm. The peak amplitude recovery in the S synthetic test of ~65-70% is lower than the ~80% recovery in the P test. We attribute this to the shorter wavelengths and relative abundance of teleseismic P arrivals. This effect is negligible when we use anomalies twice as large as in the synthetic test shown, but for this study the smaller anomalies are more pertinent as we are interested in mantle structures with a similar scale-length. The synthetic test results for V_P/V_S perturbations show little geometric distortion of the input structure, but greater amplitude loss compared to the P and S models (Fig. 2.6). We recover ~40% of the 4% peak-to-peak input V_P/V_S anomaly, which indicates that the inversion is likely to underestimate the magnitude of V_P/V_S heterogeneity more than P and S velocity heterogeneity (Fig. 2.6). It is clear that this type of synthetic test is optimistic in its assumptions since there is considerable evidence for both anisotropy and anelasticity is the southern California mantle (Savage and Silver, 1993; Liu et al., 1995; Polet and Kanamori, 2002; Yang and Forsyth, 2006 and 2008), there are errors in the

residual time measurements, and a banana-doughnut-like representation of travel-time sensitivity is an approximation based on an isotropic 1-D reference model with known ray path locations. For these reasons, we think that the variance reduction in the well-sampled regions of the model domain and the consistency between P and S tomography provide greater insight on inversion accuracy.

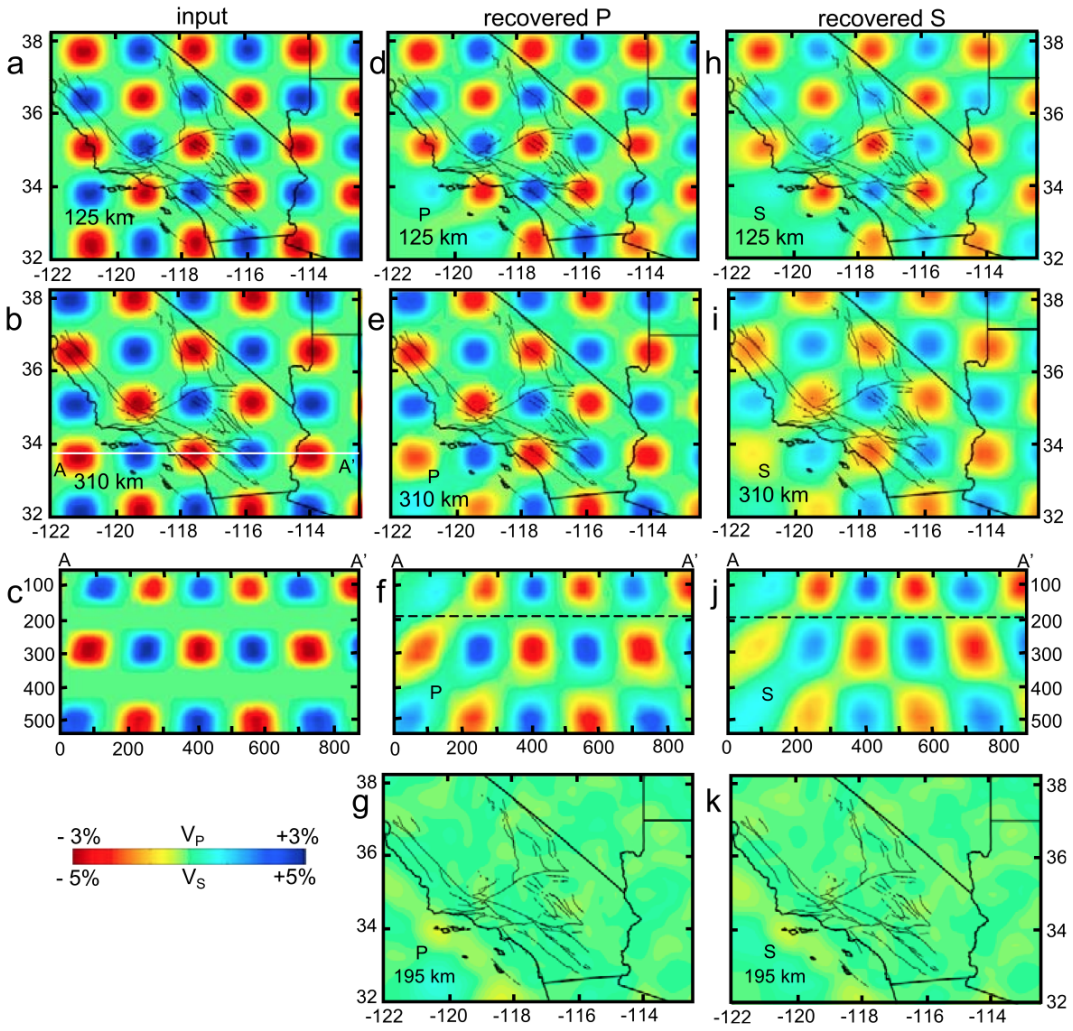

Figure 2.5. Checkerboard resolution test. (a–c) The synthetic input structure (P to ±3% and S to ±5%), (d–g) the recovered P structure, and (h–k) the recovered S structure. Map views are at the depths 125 and 310 km, as indicated. Figures 2.5c, 2.5f, and 2.5j show a cross section through the model located at the white line labeled A–A'. Figures 2.5g and 2.5k show recovered perturbations at 195 km depth, where the input structure is in between two anomalous layers and has zero perturbation.

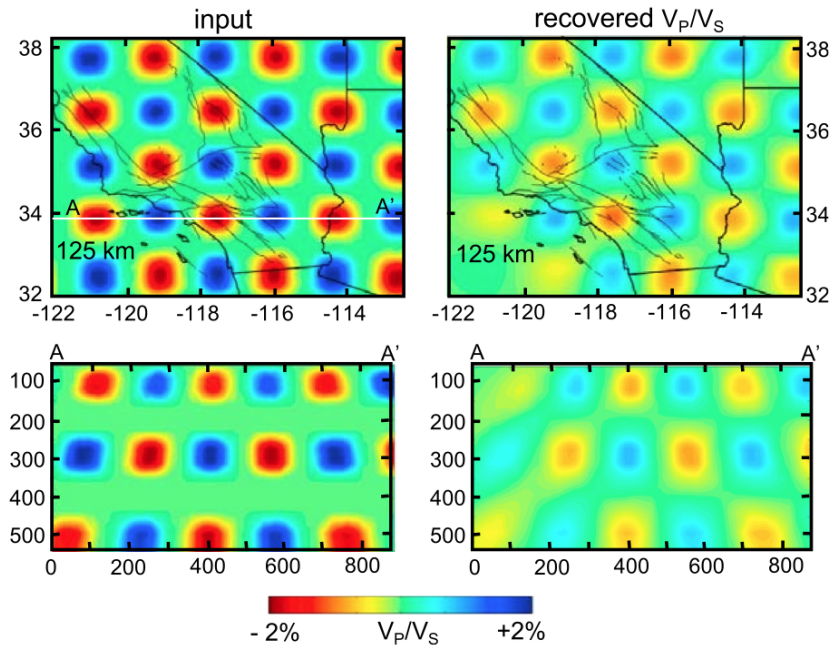

Figure 2.6. Checkerboard resolution test for V_P/V_S model. (left) The synthetic input V_P/V_S structure (±2%) and (right) the recovered V_P/V_s structure. The cross section A–A' is the same as the section in Figure 2.5.

4. Results and discussion

4.1. Inversion results

The quality of a least-squares optimal solution to an ill-posed inverse problem is commonly evaluated by the data variance reduction. Because resolution varies widely throughout the model domain and we rely on assumptions known to be invalid (such as isotropy), the overall variance reduction of a tomography model tends to be a misleading and optimistic indicator of quality. The variance reductions of the isolated P and S inversions are 85.8% and 81.6%, respectively, indicating that velocity models produced under the assumptions used can explain nearly all the observed variance in travel-time residuals. A more realistic metric of model quality is obtained by calculating the variance reduction only for portions of the model domain where resolution is greater than

some minimum threshold. Each node is assigned a "hit quality" index, ranging from 0 (for not sampled) to 1 when a node is sampled by at least 5 rays from each back-azimuth quadrant (Fig. 2.7). Our chosen threshold 0.4 (i.e., several rays from at least 2 back-azimuth quadrants), and we exclude nodes in the top layer (35 km) and bottom two layers (595 and 650 km). Both the formulation for hit-quality index and selection of the well-resolved threshold are somewhat subjective, and are chosen based on recovery of synthetic test structures (and the simple fact that rays intersecting at high angles are necessary for good resolution when back-projecting integrated residual times).

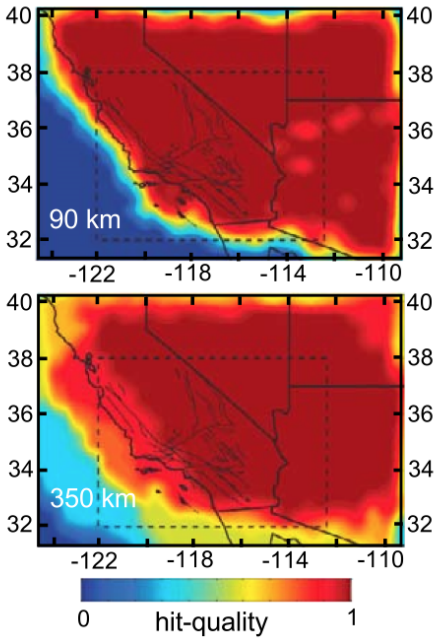

Figure 2.7. Maps of P wave hit quality. Hit quality ranges from zero for unhit nodes to one for very well hit nodes. The formula for assigning hit quality is described in above. Dashed line indicates area shown in map views in Figures 2.5, 2.6, 2.8, and 2.13.

The inversion bias to create minimum energy structure tends to cause data that cannot be explained in the well-sampled parts of our model to be expressed (artificially)

as heterogeneity in more poorly resolved volumes. Comparing the overall and well-sampled variance reduction provides an approximate metric of how much of the overall residual reduction is accounted for by structure in volumes of the tomographic model that are not well-sampled. The decrease in variance reduction from the isolated P and S inversions to the joint P and S inversion also serves to indicate the validity of our modeling assumptions. Discrepancies between the P and S datasets are likely to result from the difference in frequency bands used to measure the P and S residual times and from anisotropy as sampled by the nearly orthogonal polarization of P and S teleseismic body-waves in the upper mantle. We consider the 61.5% variance reduction in the well-sampled portion of the model from the joint P and S inversion to be the most informative indication of how well the isotropic, elastic tomography models fit the data.

4.2. V_P, V_S, and V_P/V_S heterogeneity

Strong V_P, V_S, and V_P/V_S heterogeneity is prevalent throughout the southwestern U.S. upper mantle and the magnitude of heterogeneity is too great to be explained solely by temperature variations. The amplitude of heterogeneity is greatest in the upper 200 km, the P and S models are broadly consistent, and the velocity and V_P/V_S perturbations are generally negatively correlated (Fig. 2.8). Peak-to-peak variations in V_P, V_S and V_P/V_S in the well-resolved model space and excluding the most anomalous 1% of model nodes are 7.2%, 12.5%, and 6.25%, respectively. We use the scalings from Karato [1993] and the Q values mentioned in section 2.2 to evaluate the hypothesis that the imaged velocity variations are caused entirely by temperature. The peak-to-peak V_P and V_S variations then imply respective temperature variations of 770 K and 730 K, respectively. These variations are considerably greater than the ~500 K difference

between platform lithosphere and asthenosphere at 100 km depth predicted by Nataf and Ricard [1996]. Based on heat flow measurements, Humphreys and Hager [1990] estimated the temperature at the base of 30 km thick southern California crust to be ~800 C. If we assume a typical asthenosphere potential temperature of ~1350 C, then at depths of 60 – 200 km temperature variations greater that 500 K are unlikely and variations greater than 700 K seem implausible, even in the presence of active small-scale lithospheric convection. Strengthening this conclusion is an awareness that the regularized travel-time inversions underestimate the true magnitude of velocity variations, leading to even greater estimated temperature variations.

In addition to temperature variations, varying degrees of partial melt, melt depletion, hydration, and radial anisotropy are potential causes of the 4-6% peak-to-peak V_P/V_S perturbations commonly imaged in the upper 200 km. Lateral variations in radial anisotropy could be artificially mapped into V_P/V_S perturbations because sub-vertically propagating P and S body-waves are approximately orthogonally polarized in the upper 200 km of the mantle. Joint analysis of long-period Rayleigh and Love waves (Polet and Kanamori, 1997) shows that S_H is generally faster than S_V in the southern California upper mantle. We take this as an indication that olivine a axes are preferentially organized in horizontal planes beneath southern California, which is consistent with the prevalence of SKS splitting in the region (Savage and Silver, 1993; Liu et al., 1995; Polet and Kanamori, 2002). If there are anomalous local volumes where olivine a axes are dominantly vertically oriented, which seems plausible in lithospheric drips undergoing vertical strain, this could be mapped into a V_P/V_S anomaly. However, the seismic velocity of olivine as a function of elastic wave propagation direction (Karato, 2009)

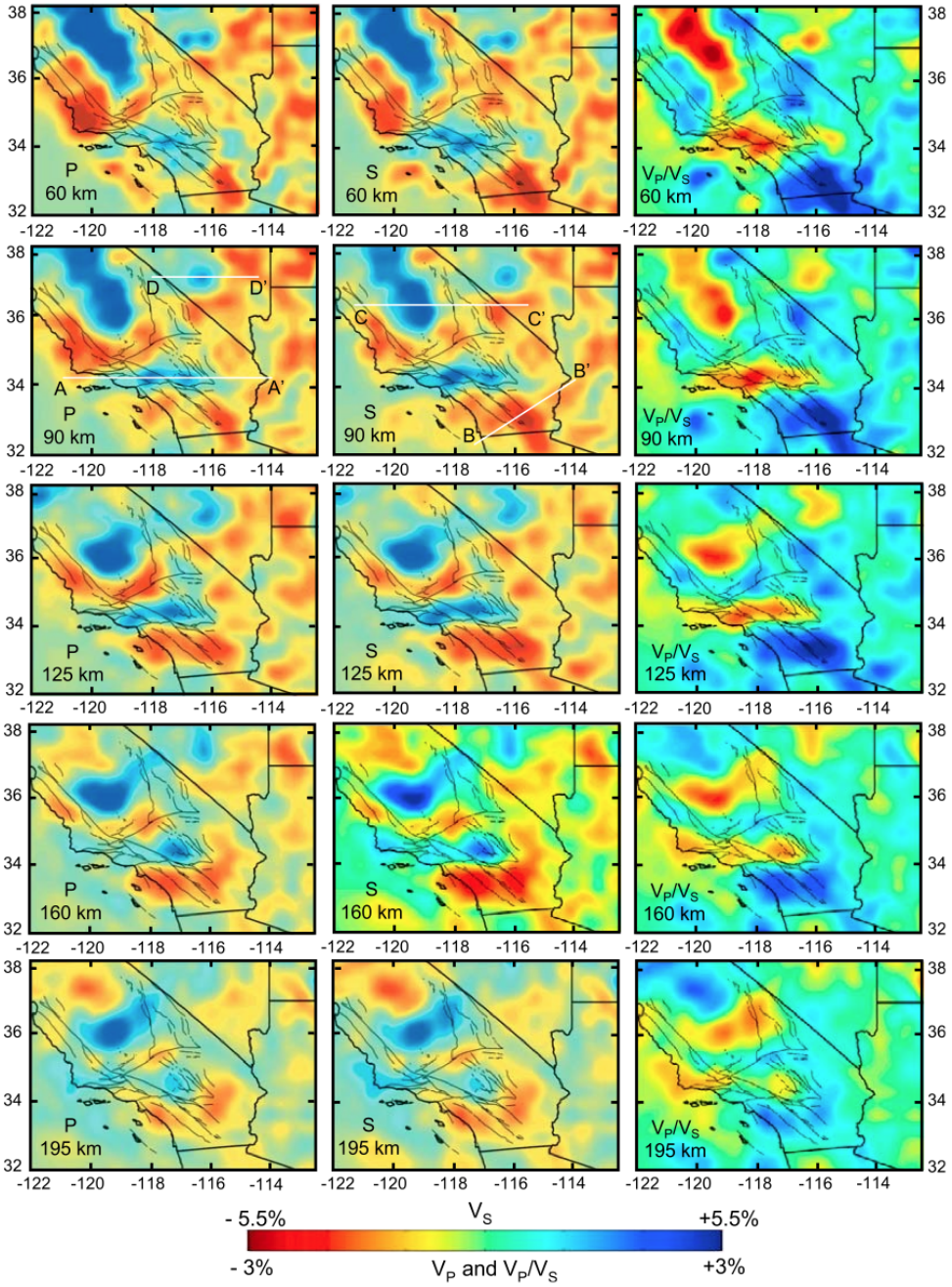

Figure 2.8. Tomography maps. Map slices from the V_P, V_s, and V_P / V_s tomograms for the joint V_P and V_s inversion. Locations of cross sections A–A' (Figure 2.10), B–B'(Figure 2.10), C–C' (Figure 2.12), and D–D' (Figure 2.11) are indicated.

indicates that V_P/V_S as sampled by steep body-wave paths should be relatively high in features with vertically oriented a axes, and we generally find relatively low V_P/V_S in

high-velocity bodies interpreted to be lithospheric drips. Because lateral variations in mantle radial anisotropy are not constrained, we are unable to quantify the potential effects on our V_P/V_S results, but it does not seem plausible that variations in radial anisotropy are the dominant cause of the strong V_P/V_S heterogeneity we image. There is not consensus as to how strongly melt depletion affects V_P/V_S (Lee, 2003; Schutt and Lesher, 2006), but depletion is generally thought to lower V_P/V_S at least slightly and is unlikely to account for the magnitude of variations we find in southern California. Hydration of the southern California asthenophere has been suggested (Yang and Forsyth, 2008), but lateral variations in hydration are also unlikely to account for the large magnitude of V_P/V_S variations. Jacobsen et al. [2009] find only 0.3% reduction in V_P/V_S for hydrous forsterite with 0.9 wt% H_2O at deep upper mantle pressure (12 GPa), and water solubility is much lower at shallower depths so we expect the effects of hydration on the velocity of sub-solidus mantle to be relatively small. In the context of upper mantle seismic velocity anomalies, the most important effect of hydration is that it enables decompression melting at greater depth than in dry peridotite because partial melt strongly effects seismic velocity and V_P/V_S (Hammond and Humphreys, 2002). Given that the 1-D velocity structure of the southern California upper mantle is anomalously slow (Polet and Kanamori, 1997; Yang and Forsyth, 2006) even with respect to the slow upper mantle of the tectonically active western U.S. (Grand and Helmberger, 1984) and the fact that the highest V_P/V_S values are found in the lowest relative velocity volumes, the presence of partial melt in the lowest velocity volumes is our preferred explanation for the large magnitude of V_P/V_S variations.

In principle, relative V_P and V_S variations can indicate the presence of partial melt. Thermal perturbations are expected to cause $\delta ln V_S / \delta ln V_P$ of ~1.65 (section 2.2), whereas partial melt is predicted to cause $\delta ln V_S / \delta ln V_P$ values of 1.6–2.4, depending primarily on the geometry of partial melt (Schmeling, 1985; Faul et al., 1994; Hammond and Humphreys, 2000), with the lowest $\delta ln V_S / \delta ln V_P$ values assuming ellipsoidal melt inclusions. Thermodynamic theory (Bulau et al., 1979) and experimental observations (Faul et al., 1994) suggest that at the low melt fractions expected in the upper mantle partial melt exists in triple junction tubules or more cuspate film-like inclusions, which have $\delta ln V_S / \delta ln V_P$ values of 1.8-2.4. We estimate regional $\delta ln V_S / \delta ln V_P = 1.84$ using regression analysis for the slope of $\delta ln V_S / \delta ln V_P$ on the nodes in the well-resolved portion of the jointly inverted model (Fig. 2.8). This estimate is greater than that derived from regression analysis of the raw residuals, 1.58. We think the difference is a result of integrated sampling of 3-D heterogeneity where the greatest magnitude of $\delta ln V_S / \delta ln V_P$ variations occurs over only a small fraction of the total ray length. Synthetic tests suggest that the $\delta ln V_S / \delta ln V_P$ estimate based on the joint inversion is an underestimate because the S model has weaker amplitude recovery. Thus, regional $\delta ln V_S / \delta ln V_P$ is expected to be somewhat greater than 1.84 and we are lead to conclude that $\delta ln V_S / \delta ln V_P$ in the southern California upper mantle is more consistent with the presence of variable partial melt content in addition to large temperature variations.

The existence of partial melt to depths as great as 150-200 km, as we infer, requires some volatile content in the southern California upper mantle. Recently, Yang and Forsyth [2008] suggested hydration of the regional asthenosphere based on modeling of Rayleigh-wave velocity and attenuation, and elevated water content seems reasonable

considering the long and complicated subduction history beneath southern California. In this case, the strong lateral variations in V_P, V_S and V_P/V_S are thought to have a significant contribution owing to the juxtaposition of cool, melt-free lithosphere against a partially molten asthenosphere as a result of variable lithospheric thickness and active small-scale convection.

Applying the Karato [1993] temperature derivatives and aforementioned Q values, and assuming the maximum lateral temperature variation in the upper mantle is 500 K, we estimate the partial melt fraction needed to explain the peak-to-peak velocity and V_P/V_S variations. One percent melt fraction is thought to increase V_P/V_S by 3-5% and decrease V_P and V_S by 2.1-3.6% and 4.3-7.9%, respectively (depending melt geometry, Hammond and Humphreys, 2000). A 500 K temperature variation corresponds to variations of 3% V_P/V_S, 5% V_P, and 8% V_S. This leaves unaccounted 2.2% in P, 4.5% in S and 3.25% in V_P/V_S, which can all be explained by 0.6-1% melt fraction in the asthenosphere. This interpretation is in agreement with the physical state inferred by Yang and Forsyth [2008], who favor a slightly hydrated asthenosphere with <1% partial melt extending from the base of the ~70 km thick lithosphere to ~200 km depth.

Thus, based on the magnitude of velocity variations and best-fit $\delta ln V_S/\delta ln V_P$ in the upper mantle we conclude that non-thermal effects, most importantly <1% partial melt in the upper 200 km, contribute significantly to seismic velocity variations. To obtain a more constrained assessment of the physical causes of seismic structure, regional constraints on 3-D attenuation in addition to V_P and V_S variations will be important.

4.3. Upper mantle seismic anomalies

A number of previous studies have imaged most of the prominent anomalies beneath southern California. Our comprehensive regional tomography provides improved spatial and amplitude resolution and, by considering P and S waves simultaneously, greater constraint on the physical properties of the mantle structures.

The approximately east-west trending high-velocity body beneath the Transverse Ranges is imaged extending from depths of ~60-75 km to ~210 km in the eastern Transverse Ranges and to ~175 km in the western Transverse Ranges (Fig. 2.9 and 2.10). These depth extents are more consistent with surface-wave tomography (Yang and Forsyth, 2006) than previous body-wave images, but the maximum depths remain ~25-50 km deeper in our body-wave images. We expect that a small amount of vertical streaking, approximately one node spacing (35 km) is inherent to the body-wave tomography even with optimal ray path coverage, and because Rayleigh wave periods sensitive to 150-200 km depth average over large lateral distances (~200-400 km) we also expect that the surface-wave tomography is likely to slightly underestimate the depth extent of such small-scale structures. Thus, the true depth extent is probably between the two estimates. Consistent with the idea that the high-velocity Transverse Ranges anomaly represents downwelling lithosphere (Humphreys et al., 1984; Bird and Rosenstock, 1984; Kohler, 1999), the velocity contrast between the Transverse Ranges anomaly and surrounding mantle increases from 60 to 90 km depth, which is near the base of the ~70-80 km thick southern California lithosphere (Li et al., 2007; Yang and Forsyth, 2008; A. Levander, pers. comm.). The average north-south thickness of this anomaly is ~50 km, and it appears to be thinnest near its intersection with the surface

trace of the San Andreas Fault. We note that the travel-time anomaly appears to be continuous in maps of P-wave residual times from the densely spaced short period network and the first Fresnel zones of these waves are smaller than the node spacing. This leads us to suggest that the Transverse Ranges anomaly is likely continuous beneath the San Andreas Fault (SAF) and its north-south thinning beneath the SAF is sufficient to cause distinct anomalies in the surface-wave image. The high-velocity anomaly beneath the Transverse Ranges (and other sub-lithospheric high-velocity anomalies) is relatively low in V_P/V_S. We suspect this primarily results from contrast with a damp, partially molten regional asthenosphere rather than unusually low absolute V_P/V_S values within the Transverse Ranges anomaly.

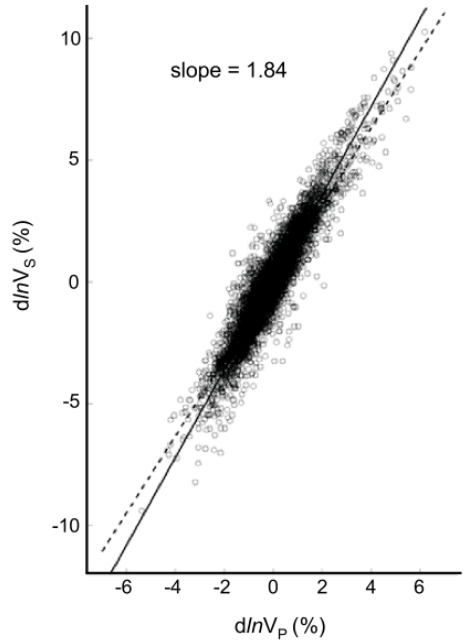

Figure 2.9. Regression analysis of model parameters. The best fit line to the dlnVp and dlnVs values has a slope of 1.84 (solid line) with a bootstrap standard error of 0.05, and the slope predicted by regression analysis of the traveltime residuals (from Figure 1.3) is 1.58 (dashed line).

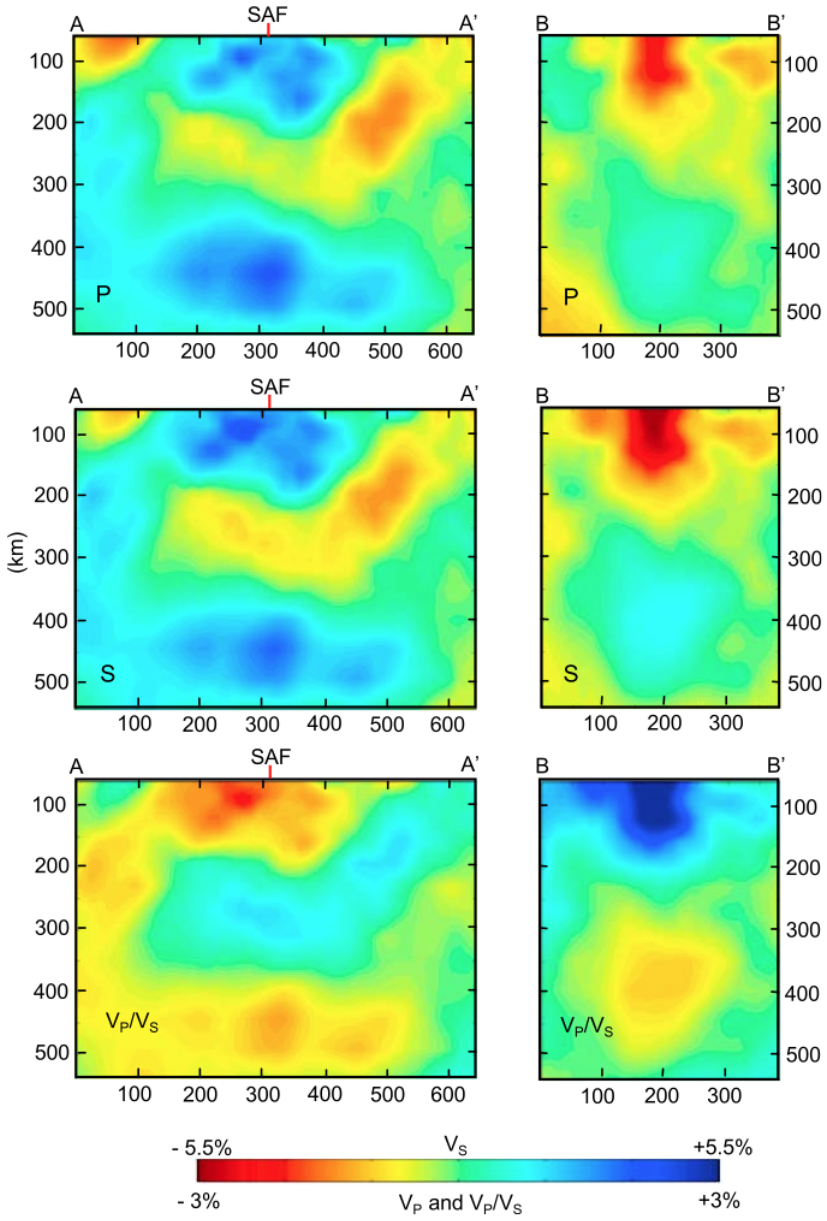

Figure 2.10. Tomography cross-sections. Cross sections through the (left) Transverse Ranges and (right) Salton Trough, located as cross sections A–A' and B–B' in Figure 2.8. Location of the San Andreas fault (SAF) indicated.

The most anomalous and laterally extensive high V_P/V_S volume is the upper 200 km of the California mantle south of the Transverse Ranges (Fig. 2.10). Although this anomaly is strongest beneath the Salton Trough, where we find V_P/V_S perturbations of

+3.5% (Fig. 2.10), high V_P/V_S values are found between 60-200 km depth beneath nearly all of southernmost California (except near the U.S.-Mexico border beneath the Peninsular Ranges). The amplitude of this low-velocity, high V_P/V_S anomaly decreases rapidly below ~150 km. Partial melting, and hence relatively high V_P/V_S, is expected beneath the Salton Trough, where oblique lithospheric spreading drives mantle ascent. However, the lateral extent and continuity of this high V_P/V_S anomaly require another explanation. It would be most easily explained with locally thinner lithosphere (and increased amounts of decompression melting in the underlying asthenosphere). Recent S receiver function analysis images the lithosphere-asthenosphere boundary (LAB) in this area to be ~15 km shallower than the average southern California depth of ~80 km, and the LAB to be ~25 km shallower than average beneath the Salton Trough.

In the upper 60-90 km of the mantle between the Carrizo Plain segment of the SAF and Point Arguello there is a low-velocity anomaly that is particularly strong in the P model (Fig. 2.8). The highest amplitude portion of the anomaly lies beneath a small gap in station coverage, hence we expect that shallow mantle resolution is not as good as in most of southern California. However, most of the lateral extent of this low-velocity anomaly is very well sampled. The low velocities may be a result of changes in lithospheric structure west of the SAF or upwelling of asthenosphere related to the nearby Isabella anomaly.

A high-velocity anomaly ~50-75 km in diameter is imaged beneath southwestern Nevada from ~60-175 km depth (Fig. 2.9 and 2.11). This anomaly has been identified previously (Spence, 1974; Monfort and Evans, 1982; Biasi and Humphreys, 1992). The high-velocity structure lies beneath the Timber Mountain volcanic field, which produced

large volumes of rhyolitic lavas and tuffs ~15-10 Ma, followed by smaller volumes of basaltic lava erupted sporadically since 10 Ma (Crowe et al., 1983; Christiansen and Yeats, 1992). P-wave resolution in this area is superior to S-wave resolution because we use abundant P data from a local short-period array in addition to TA data. The relatively low V_P/V_S value is not very well constrained because the dense P-wave dataset dominates the sparse S-wave dataset in this area. Possible origins for this structure are melt depletion-related dehydration of the asthenosphere and lithospheric downwelling.

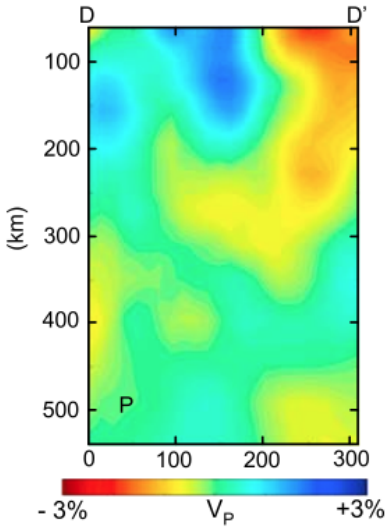

Figure 2.11. Timber Mountain anomaly cross-section. Location is cross section D–D' in Figure 2.8.

The well-known and very strong high-velocity Isabella anomaly (maximum of +5% P and +8.5% S) lies beneath the southern Great Valley and Sierra Nevada [Fig. 2.9, 2.12] (Zandt et al., 2004; Boyd et al., 2004). This structure extends continuously from near the base of the lithosphere beneath southern Great Valley to ~300 km depth beneath the eastern Sierra Nevada and Owens Valley (Fig. 2.12). This maximum depth of the

anomaly is greater than the ~230 km depth previously inferred by body-wave studies (Biasi and Humphreys, 1992; Benz et al., 1992; Boyd et al., 2004), and ~100 km deeper than the maximum depth imaged by Rayleigh-wave tomography (Yang and Forsyth, 2006). Crossing ray coverage in this area is excellent so we expect our body-wave results are robust, and reconciling the difference with the surface-wave tomography remains a challenge. The Isabella anomaly is largely surrounded by anomalously low-velocity mantle in the 90-160 km depth range, and at depths near the base of the lithosphere (60–90 km) we also find high-velocity mantle beneath most of the Sierra Nevada and western Sierra foothills.

An east-west elongated high-velocity anomaly is imaged in the deep upper mantle beneath the California borderland and much of southwestern California (Fig. 2.12, 2.13). Its amplitude (~2% P) and lateral extent (~400 km by ~200 km) are greatest from 325-475 km depth. Sigloch et al. [2008] find a high-velocity (~>0.5% P) body deeper beneath southern California at approximately 400-700 km depth. Our model resolution in this area not optimal because stations are not available far to the south or west of the anomaly, but some crossing ray coverage is provided by the island stations directly above the anomaly in the borderlands and the dense SCSN array on the mainland. Resolution tests suggest that we can be confident a significant high-velocity anomaly exists, but the geometry of the structure may be somewhat distorted, particularly at its western end. However, it also is possible that out-of-box heterogeneity influences the imaged structure at this location. The existence of this large, high-velocity anomaly at such depths is intriguing considering subduction terminated beneath this area ~25 Ma. In an absolute

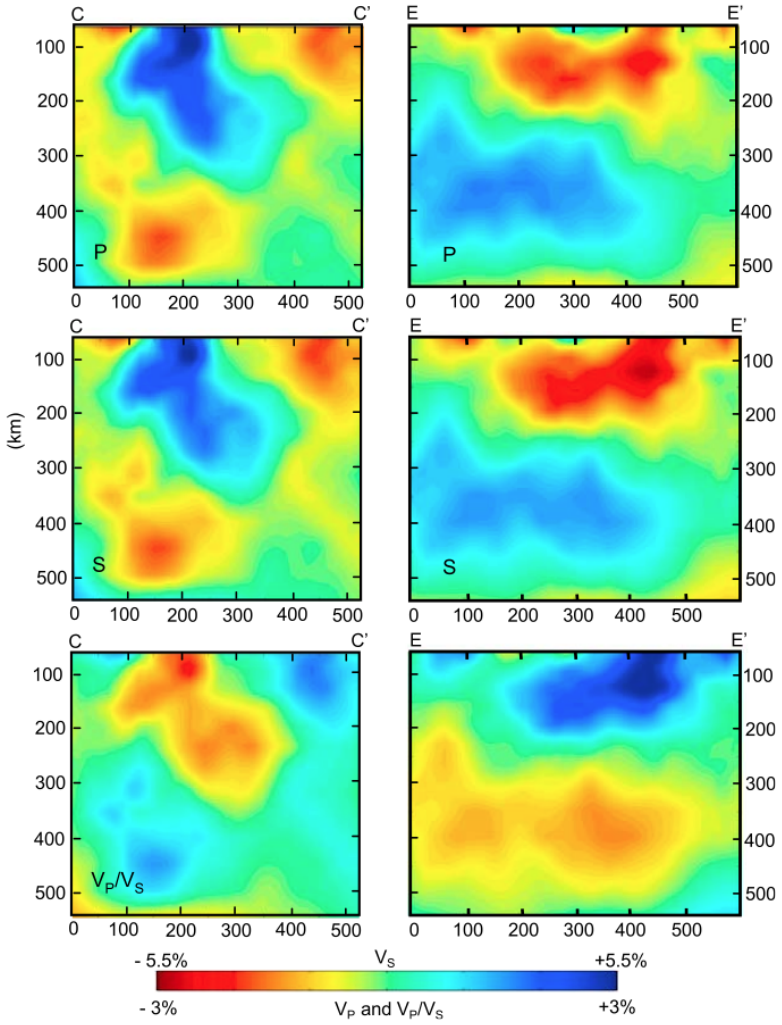

Figure 2.12. Tomography images. (left) Southern Great Valley and southern Sierra Nevada cross section located as C–C' in Figure 2.8. (right) Deep, high-velocity upper mantle anomaly beneath southern California. Cross section E–E' is labeled in Figure 2.13. This feature is continuous with the slightly deeper high-velocity anomaly beneath the Transverse Ranges shown in Figure 2.10.

reference frame, North America has moved ~1000 km to the southwest since that time (Engebretson et al., 1985) and geodynamic modeling suggests eastward directed asthenospheric flow beneath the region (Becker and O'Connell, 2001). Consequently, one would expect any deep products of subduction beneath southern California to be located farther east, beneath the interior of the continent.

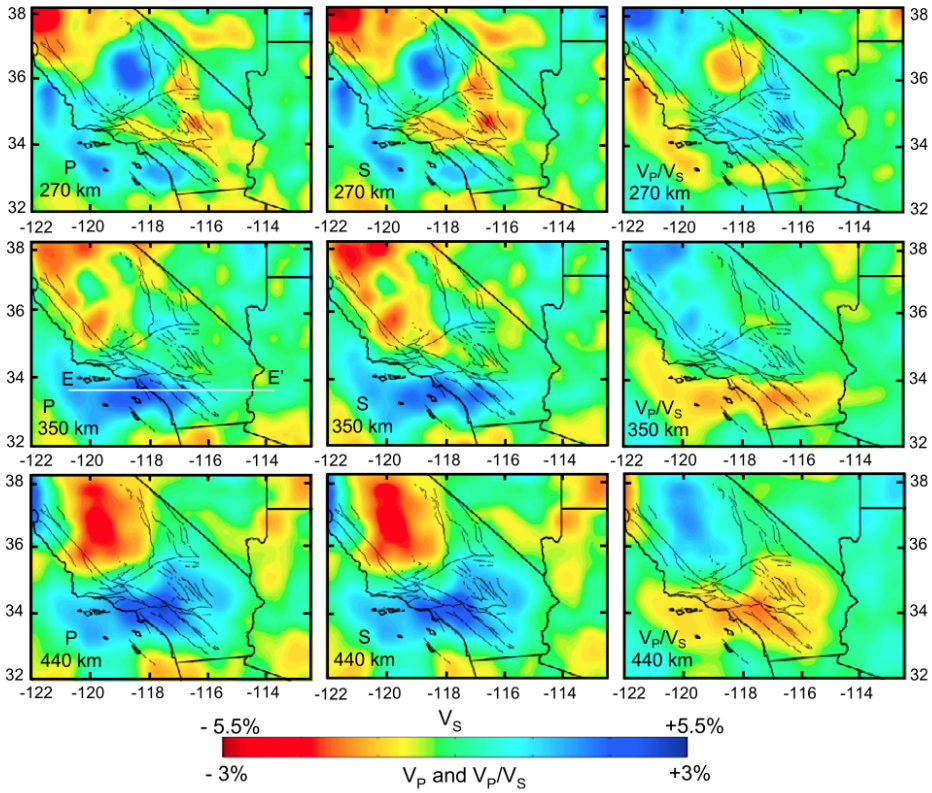

Figure 2.13. Map slices of the deep upper mantle. Vp, Vs, and Vp/Vs tomograms for the joint Vp and Vs inversion. Location of cross section E–E' (Figure 2.12) is indicated.

5. Conclusions

We have inverted teleseismic P and S body-wave data for 3-D variations in V_P, V_S, and V_P/V_S in the southern California upper mantle. Use of nearly all available teleseismic body-wave data in the southwestern U.S., regional crust thickness and velocity models, and multiple-frequency inversion of P and S travel-time residuals, provide a new level of constraint on regional upper mantle seismic structure. Joint inversion of the P and S datasets is achieved by a simple requirement of smooth $\delta\ln V_P$, $\delta\ln V_S$, and $\delta\ln V_S/\delta\ln V_P$ fields, and provides insight into the causes of seismic heterogeneity. The velocity and V_P/V_S perturbations are generally negatively correlated

and the highest V_P/V_S and lowest velocity values are found in areas where we expect ascending asthenosphere and relatively thin lithosphere. In the upper 200 km, the large magnitude of P and S velocity variations, high mean $\delta \ln V_S / \delta \ln V_P$, and knowledge that the average regional upper mantle is very slow (even relative to the tectonically active western U.S.), lead us to conclude that lateral variations in partial melt content contribute significantly to observed seismic heterogeneity. Consequently, commonly used velocity-density scalings based solely on thermal effects would tend to over-estimate density variations and the magnitude of crustal loads that result from small-scale upper mantle convection. This highlights a need for further advances in 3-D seismic imaging that simultaneously resolves V_P, V_S, attenuation and anisotropy structure; our work represents an important step in this direction. With improvements to seismic resolution and velocity-density scaling, especially when combined with joint seismic-gravity modeling, we will obtain better constraint on the actual density structure and therefore the role of small-scale convection in southern California tectonics and fault stress levels.

This chapter presents a tomographic imaging method and its implementation with travel-time data primarily from southern California. In the following chapter the imaging method is implemented with newly available data covering the entire western U.S. The resulting images provide unprecedented insight into mantle structure beneath the broadly uplifted and tectonically and magmatically active western U.S. Cordillera.

CHAPTER III

COMPLEX SUBDUCTION AND SMALL-SCALE CONVECTION REVEALED BY BODY-WAVE TOMOGRAPHY OF THE WESTERN U.S. UPPER MANTLE

This work was published in volume 297 of Earth and Planetary Science Letters in 2010. Coauthor Eugene Humphreys provided guidance in the analysis, interpretation, and editorial process. I performed all analysis and was the primary author of the manuscript.

1. Introduction

The western United States provides an excellent region for advancing our understanding of mantle heterogeneity caused by subduction (Sigloch et al., 2008), small-scale convection of the lithosphere (Bird, 1979; Zandt et al., 2004), and plumes (Schutt and Dueker, 2008; Smith et al., 2009) both because these processes appear to be active there and because the seismic data are unparalleled. In particular, the transportable array (TA) component of EarthScope's USArray is providing a fundamental advance in data coverage, allowing for continuous high-resolution imaging from the Pacific coast to the western Great Plains. Seismologists have long recognized that subduction beneath western U.S. occurs into an anomalously low-velocity upper mantle (Romanowicz, 1979; Grand, 1994); on average, mantle seismic velocities between 100-200 km depth are among the lowest on Earth (Lebedev and van der Hilst, 2008). Imaged within this generally low-velocity mantle are small-scale high-velocity structures that exhibit seismic contrasts as great as that observed between average craton and the tectonically active western U.S. (Humphreys and Dueker, 1994). That the western U.S. upper mantle is

vigorously active is implicated by geologic study, which has shown that the western third of the U.S. is undergoing post-Laramide orogenic collapse with accompanying volcanism (Coney and Harms, 1984; Burchfiel et al., 1992), and it has been uplifted into one of Earth's great plateaus. The elevated western U.S. interior is comprised of distinctive tectonic and geomorphic provinces (Fig. 3.1), including the highly extended and magmatically altered Basin and Range, the Laramide-contracted and unextended Colorado Plateau and Rocky Mountains, and the tilted and intact Great Plains. It appears that large portions of the Great Plains, Rocky Mountains and Colorado Plateau have been uplifted in part since the Laramide orogeny (Heller et al., 2003), with evidence for uplift continuing to the present (Riihimaki et al., 2008; Karlstrom et al., 2008). This indicates young and ongoing mass redistribution at depth.

Ongoing transition of the westernmost North America plate margin from subduction to transform (Atwater, 1970) has been used to predict a triangular slab-free area beneath most of the Basin and Range and southern Rocky Mountains (Dickinson and Snyder, 1979), although geologic evidence for complex subduction since ~80 Ma suggests that the actual slab distribution may be more complicated than that predicted by plate kinematics. In particular, the distribution of Laramide thrust faulting and magmatism suggests flat-slab subduction as far inboard as the Rocky Mountain Front (Bird, 1984), and the subsequent ignimbrite flare-up of the Basin and Range is thought to represent slab removal (Coney and Reynolds, 1977) beneath the Basin and Range (Humphreys, 1995). Accretion of the Siletzia ocean lithosphere ~50 Ma in the northwestern U.S. necessitated slab tearing and initiation of subduction at Cascadia (Humphreys, 2009). The fate and distribution of ~5000 km of slab subducted since 80 Ma

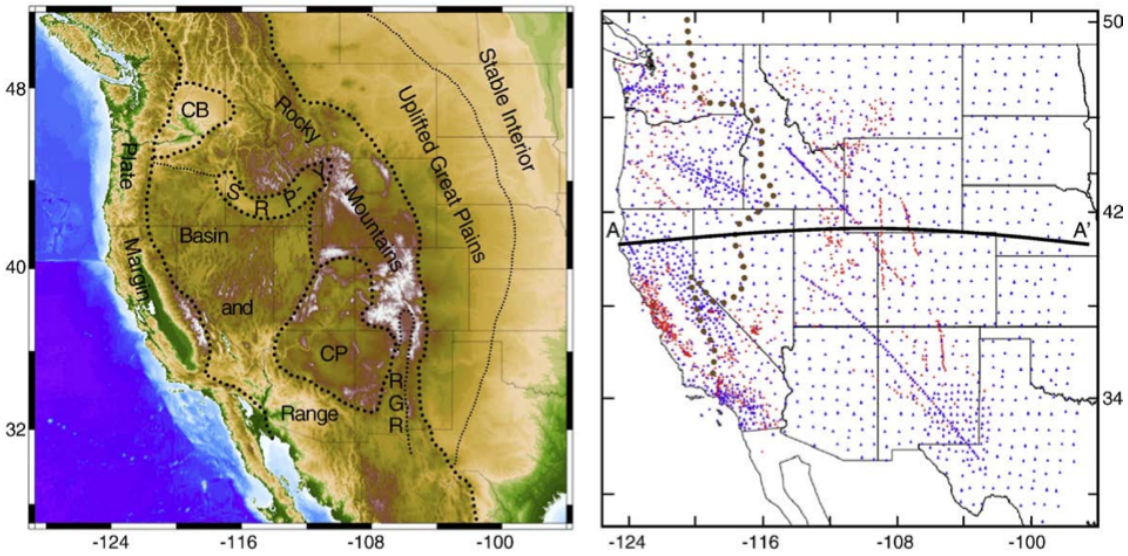

Figure 3.1. Regional geography and station map. Major geologic provinces of the western U.S. are labeled on the left map abbreviated names include the Columbia Basin (CB), Snake River Plain–Yellowstone hotspot track (SRP–Y), Colorado Plateau (CP), and Rio Grande Rift. The right map shows the stations used only for P data (red) and stations used for both P and S data (blue). We include TA data up to December 2009. The 0.706 Sr line (brown dotted) indicates the approximate boundary between accreted oceanic terranes to the west and Precambrian North America to the east (from DeCelles, 2004). The location of cross-section A–A′ used for the synthetic test results in Fig. 3.3 is indicated.

is the subject of several recent seismic investigations (Sigloch et al., 2008; Burdick et al., 2009; Roth et al., 2008, Tian et al., 2009, Xue and Allen, 2010).

In this paper we present new travel-time tomography models of 3-D V_P, V_S, and V_P/V_S perturbations in the western U.S. upper mantle. Use of nearly all available teleseismic body-wave data and recently advanced crustal models results in upper mantle resolution superior to previous efforts, and imaging of V_P/V_S perturbations helps identify where properties other than temperature have a strong influence on seismic structure.

2. Data and methodology

2.1. Travel-time data

We use relative travel-time residuals of teleseismic P and S phases observed at 2661 seismic stations (1648 stations for S) in the western U.S. to invert for 3-D perturbations in upper mantle V_P, V_S, and V_P/V_S (Fig. 3.1). Direct P and PKP phases observed on the vertical component are used for P-wave residuals. S-wave data are rotated to radial and tangential components and residuals are measured for direct S observed on the tangential component and SKS observed on the radial component. Residual times are measured by cross-correlation of band-pass-filtered waveforms in up to four Gaussian frequency bands with center frequencies of 1, 0.5, 0.3, 0.1 Hz for P-waves and 0.4, 0.1, 0.05 Hz for S-waves. Data from short-period stations are only used for 1 Hz P residuals. In total, we use 248,000 P residuals (47% 1 Hz, 26% 0.5 Hz, 22% 0.3 Hz, 5% 0.1 Hz) and 84,000 S residuals (6% 0.4 Hz, 52% 0.1 Hz, 42% 0.05 Hz). We prefer to use more high-frequency data in the inversions because these data sample the mantle over smaller length-scales, there is dense station spacing in the region, and residual time uncertainty increases with period. However, relatively few high quality S arrivals are observed at 0.4 Hz. The root mean square (RMS) values of the P and S residuals are 0.43 s and 1.18 s, respectively. The mean of the travel-time residuals must be zero because we use relative times; consequently, we cannot constrain the mean 1-D velocity structure beneath the western U.S.

We use topography and crustal velocity and thickness models to calculate ray theoretical travel-time corrections for crustal heterogeneity. We expect that frequency-

dependence of crust correction times (Ritsema et al., 2009) is small for the phases and frequencies in our relative travel-time dataset. Recent results using TA data constrain variations in crust thickness (Gilbert and Fouch, 2007) and velocity (Yang et al., 2008; Lin et al., 2008) across the western U.S. These results serve as a background model, which is replaced by higher-resolution local models that cover most of California (Tape et al., 2009; Thurber et al., 2008) and the Yellowstone region (Stachnik et al., 2008). For most of the western U.S. only V_S crustal models derived from dispersion of diffusive Rayleigh waves are available (Yang et al., 2008; Lin et al., 2008) and we assume a mean crustal V_P/V_S of 1.74 (Chulick and Mooney, 2002) to calculate correction times for P arrivals. This simple scaling of V_S to V_P will introduce some error, but these errors are small compared to the errors that would be introduced by ignoring strong crustal structures such as basins and crystalline mountain ranges. The respective P and S crust time corrections have RMS values of 0.11 and 0.18 s, with ~65% of the RMS resulting from crust thickness variations. After correction, the RMS of the P and S residuals is 0.41 and 1.15, respectively. That the RMS of the residual times is approximately the same after crust corrections indicates that there is not a simple correlation between the crust structure and integrated travel-time residuals. This observation cautions against relying solely on inversion-based station terms to correct for crust structure, because station terms effectively reduce the magnitude of travel-time residuals and would therefore lead to diminished recovery of mantle heterogeneity.

Linear regression of P and S residuals for common stations and events provides an estimate of ray path integrated $\delta ln V_S / \delta ln V_P$ in the region. The linear fit with a slope of 2.84 minimizes a weighted sum of the squared errors, which accounts for uncertainties in

P and S residuals (Fig. 3.2) estimated following VanDecar and Crosson [1990]. Using station terms from fewer and more irregularly distributed stations in the western U.S., Romamowicz and Cara [1980] found a slope of 2.54. Our best-fit slope, 2.84, corresponds to $\delta ln V_S / \delta ln V_P$ of 1.57 assuming an average upper mantle V_P/V_S of 1.81 as in AK135 (Kennett and Engdahl, 1995). Mantle temperature variations are predicted to produce $\delta ln V_S / \delta ln V_P$ of 1.2 – 2 (Anderson et al., 1992; Goes et al., 2000) depending primarily on the assumed attenuation structure. To account for the anelastic contribution of temperature variations we assume mean upper mantle Q_S of 100 and negligible bulk attenuation to calculate mean Q_P of 225. The assumed Q values are guided by the Rayleigh-wave attenuation study of Yang and Forsyth [2008] who find mean Q_S of ~95 in the upper 200 km of the southern California mantle, and a recent global study (Dalton et al., 2008) that Q_S beneath the southwest U.S. at ~100 km depth to be lower than the mean for the entire study area. Using these Q values with the scalings of Karato [1993], $\delta ln V_S / \delta ln V_P$ of ~1.6 is expected for thermal variations. Thus, it appears the residual times are consistent with temperature being the dominant cause of velocity variations. However, slope analysis of residual times is expected to underestimate *a,* and consequently $\delta ln V_S / \delta ln V_P$, because the residuals are an integrated sampling of 3-D heterogeneity in the volume about the entire ray path. Furthermore, the mean wavelength of the measured S-waves is ~2 times the mean wavelength of the P-waves so the S residuals average over larger mantle volumes and likely underestimate the magnitude of V_S variations and hence $\delta ln V_S / \delta ln V_P$. To better constrain $\delta ln V_S / \delta ln V_P$ in the presence of 3-D heterogeneity we perform a joint inversion of the P and S datasets (see section 3.2).

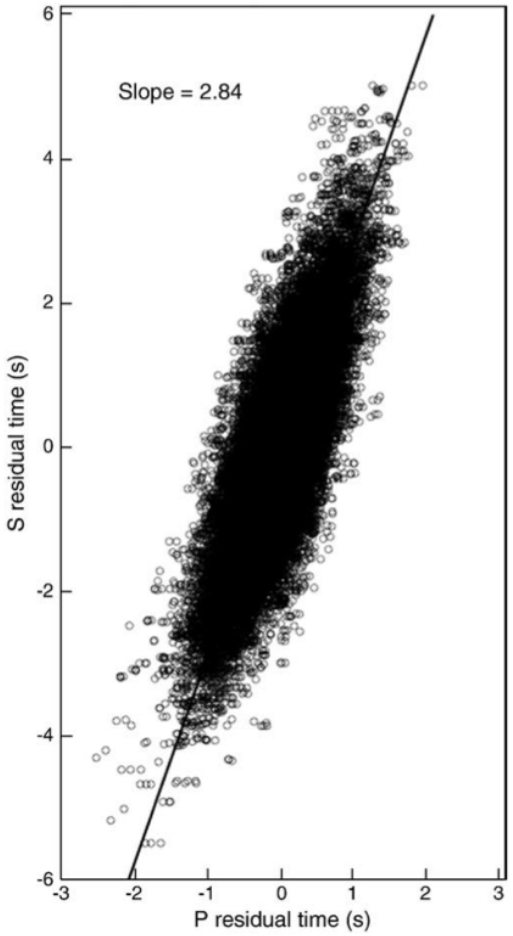

Figure 3.2. Linear regression of P and S residuals. We use 56,000 P (62% 0.3 Hz and 38% 0.5 Hz) and S (0.1 Hz) residuals from events with at least 40 common stations to estimate the value of a. Typical uncertainties for residual times are ~1/20 of the dominant period. The fit line has a slope of 2.84 with a bootstrap standard error of 0.06.

2.2. Tomographic method

We use frequency-dependent 3-D sensitivity kernels to relate travel-time residuals to perturbations of model parameters. We only consider sensitivity in the first Fresnel

zone and we use an approximation of the Born theoretical, "banana-doughnut" kernel (Dahlen et al., 2000) within the first Fresnel zone. A detailed description of the method is given in Schmandt and Humphreys [2010].

Nodes at the vertices of an irregular, rectangular 3-D mesh parameterize the model space. The model domain extends from 35 km to 1015 km depth, and the vertical distance between nodes increases gradually from 30 km (at 60-90 km depth) to 65 km (>820 km depth) to address growing first Fresnel-zone width and decreasing resolution. Horizontal node spacing is smallest beneath the interior of the TA (40 km) and gradually increases moving outward with the largest spacing (60 km) beyond the boundary of the entire array, where there is a paucity of crossing rays. Resolution is poor in the 35 km layer as a result of near vertical ray path orientation and uncertainties in the *a priori* crust model. This layer tends to absorb both errors in the crust model and crust and uppermost mantle velocity variations that are not well constrained by our data. In areas with only TA data, good crossing ray coverage is not achieved until ~80 km depth. However, because we use more than 1700 stations in addition to the TA (>700 for S data) there is good crossing ray coverage in the 60 km layer throughout much of the western U.S.

In addition to the V_P and V_S model parameters, we invert for station and event parameters. Because we correct for crust thickness and velocity variations, the station terms are only intended to address local site effects and errors in the *a priori* crust model; consequently, we apply strong station damping to keep the station terms from absorbing mantle structure. The RMS of the station terms is 0.05 s and 0.08 s for P and S, respectively. Event terms represent adjustment of the mean arrival time for the specific set of stations that record each event. These terms are important because we solve for

velocity perturbations rather than absolute velocity, and the mean velocity structure varies significantly for different arrays in the western U.S.

We follow the same procedure as Schmandt and Humphreys [2010] for the construction and solution of the inverse problem. In addition to separate V_P and V_S inversions we also jointly invert the P and S datasets for V_P/V_S variations by simultaneously imposing a smoothness constraint on $\delta ln V_S$, $\delta ln V_P$, and $\delta ln V_S/\delta ln V_P$ fields (similar to Hammond and Toomey, 2003). Thus, deviations from the reference V_P/V_S values of AK135 are not penalized, but roughness is penalized. The P and S datasets are equally weighted in the joint inversion because the main motivations for the joint inversion are to explore the consistency of the two datasets and obtain better estimates of $\delta ln V_S/\delta ln V_P$ in the upper mantle.

2.3. Synthetic resolution tests

Synthetic tests demonstrate expected model resolution with the assumptions of an isotropic elastic mantle, accurate ray locations, and sensitivity limited to the first Fresnel zone. The synthetic structure consists of three checkerboard layers embedded in a neutral background (Fig. 3.3). In general, the recovery of the input structure in the P and S velocity models is good, although we find some streaking and amplitude loss owing to the sub-vertical orientation of teleseismic rays and the preference for minimum energy structure in the inversion algorithm. Peak P amplitude recovery generally is higher than peak S amplitude recovery, 70-80% and 60-70%, respectively. It also appears that the shorter wavelength P data more accurately recover the input structure near the margins of anomalous volumes. The synthetic test results for V_P/V_S perturbations show little

geometric distortion of the input structure, but lower peak amplitude recovery, 50-60%, (Fig. 3.3), which indicates the inversion underestimates the magnitude of V_P/V_S heterogeneity more than P and S velocity heterogeneity. In general, the P model is expected to have better resolution than the S model as a result of ~1000 more stations, shorter wavelengths of measured P waves, and the relative abundance of high quality teleseismic P arrivals from regions with lower magnitude and less frequent seismicity (i.e., more useable P arrivals from mid-ocean ridge and transform earthquakes improves ray-path distribution). Consequently, we prefer to give the structure resolved by the P data more weight in our interpretations, and hence we present more figures from the P model.

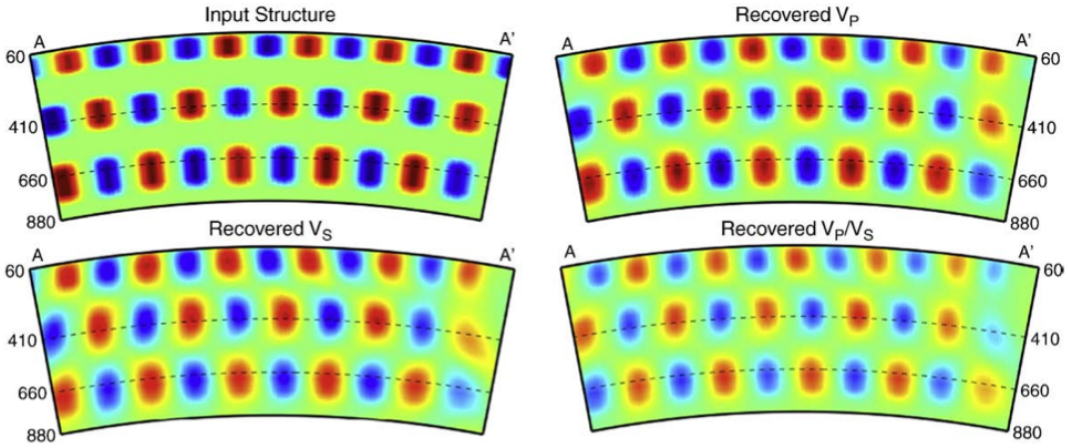

Figure 3.3. Synthetic test results. The same cross-section, labeled on Fig. 3.1 as A–A′, is shown for the input structure (upper left), recovered V_P (upper right), recovered V_S (lower left), and recovered V_P/V_S (lower right). Note that the sign of the input structure should be reversed for the V_P/V_S test, but the geometry of anomalous volumes is the same. Color scale limits for the recovered structure are the respective peak perturbations in the input structure for V_P (±3%), V_S (±5.5%), and V_P/V_S (±2.3%).

3. Results and discussion

3.1. Fit to the data

The quality of a least-squares optimal solution to an ill-posed inverse problem is commonly evaluated by the data variance reduction. Because resolution varies widely throughout the model domain and we rely on assumptions known to be invalid (such as isotropy), the overall variance reduction of a tomography model tends to be a misleading and optimistic indicator of quality. The variance reductions of the isolated P and S inversions are 87.3% and 85.6%, respectively, indicating that velocity models produced under the assumptions used can explain nearly all the observed variance in travel-time residuals. A more realistic metric of model quality is obtained by calculating the variance reduction only for portions of the model domain where resolution is greater than some minimum threshold. Each node is assigned a "hit quality" index, ranging from 0 (for not sampled) to 1 when a node is sampled by at least 5 rays from each back-azimuth quadrant and at least 5 rays from core phases. Our chosen threshold is 0.4 (i.e., several rays from at least 2 back-azimuth quadrants), and we exclude nodes in the top layer (35 km) and bottom two layers (950 and 1015 km). Both the formulation for hit-quality index and selection of the well-resolved threshold are somewhat subjective, and are chosen based on recovery of synthetic test structures (and the simple fact that rays intersecting at high angles are necessary for good resolution).

Comparing the overall and well-sampled variance reduction provides an approximate metric of how much of the overall residual reduction is accounted for by structure in volumes that are not well-sampled. The decrease in variance reduction from

the isolated P and S inversions to the joint P and S inversion also serves to indicate the validity of our modeling assumptions. Discrepancies between the P and S datasets are likely to result from differences in station density, anisotropy as sampled by the orthogonal polarization of P and S teleseismic body-waves, and the difference in frequency bands used to measure the P and S residuals. Differences between the separately inverted P and S models are more prominent at depths greater than ~300 km. At these depths, the jointly inverted P and S models are more similar to each other and to the separately inverted P model. Because the two datasets are equally weighted in the joint inversion this suggests the P data have at least slightly better resolution than the S data. We consider the 66.7% variance reduction in the well-sampled portion of the model from the joint P and S inversion to be the most informative indication of how well the isotropic, elastic tomography models can fit the data.

3.2. Seismic heterogeneity and physical state

The most striking aspect of the tomographic images is the strong multi-scale heterogeneity in the upper 200 km (Fig. 3.4). The V_P and V_S models are highly mutually consistent, and velocity and V_P/V_S perturbations are generally negatively correlated. Excluding the most anomalous 1% of model parameters, peak-to-peak amplitudes at less than 200 km depth in the well-sampled model space are 7.8% V_P, 14.5% V_S, and 7.2% V_P/V_S. This magnitude of heterogeneity is large relative to other body-wave tomography studies, but is in close agreement with surface-wave tomography studies using TA data (Yang et al., 2008; Pollitz and Snoke, 2010). Physical origins of seismic velocity variations are variations in temperature, partial melt, anisotropy, bulk and volatile composition. Seismic structure of magnitude as great that imaged must include an

important contribution from temperature. It is informative to consider the magnitude of temperature variations required if the entire peak-to-peak velocity variations are attributed to temperature change. Using the temperature derivatives of Karato [1993] and the Q values from section 2.1 the peak-to-peak V_P and V_S variations correspond to temperature variations of 850 K and 960 K for V_P and V_S, respectively. These values are very high, but perhaps possible given the potential range of lithosphere and asthenosphere temperatures in a model that spans Achaean lithosphere, Cenozoic accreted terrains, the highly extended Basin and Range, and the Yellowstone hotspot. Alternatively, a small amount of partial melt in the asthenosphere would reduce the predicted temperature variations to more reasonable values. For example, up to 0.5% partial melt in the asthenosphere would reduce the required temperature variations by ~200 K (Hammond and Humphreys, 2000). The existence of partial melt in the lowest velocity volumes seems likely considering the strong correlation with young volcanic fields and the low mean velocity of the western U.S. asthenosphere (Lebedev and van der Hilst, 2008). Strengthening the idea that non-thermal effects contribute significantly to velocity variations is an awareness that regularized travel-time inversions underestimate the true magnitude of velocity variations leading to even greater estimated temperature variations.

Aside from variations in temperature and partial melt, V_P/V_S anomalies can be caused by lateral variations in bulk and volatile composition. Two potential compositional influences on mantle V_P/V_S are hydration, whose effects on velocity are relatively modest in the shallow upper mantle where water solubility is low, and melt depletion. Hydration of the western U.S. lithosphere (Humphreys et al., 2003) and

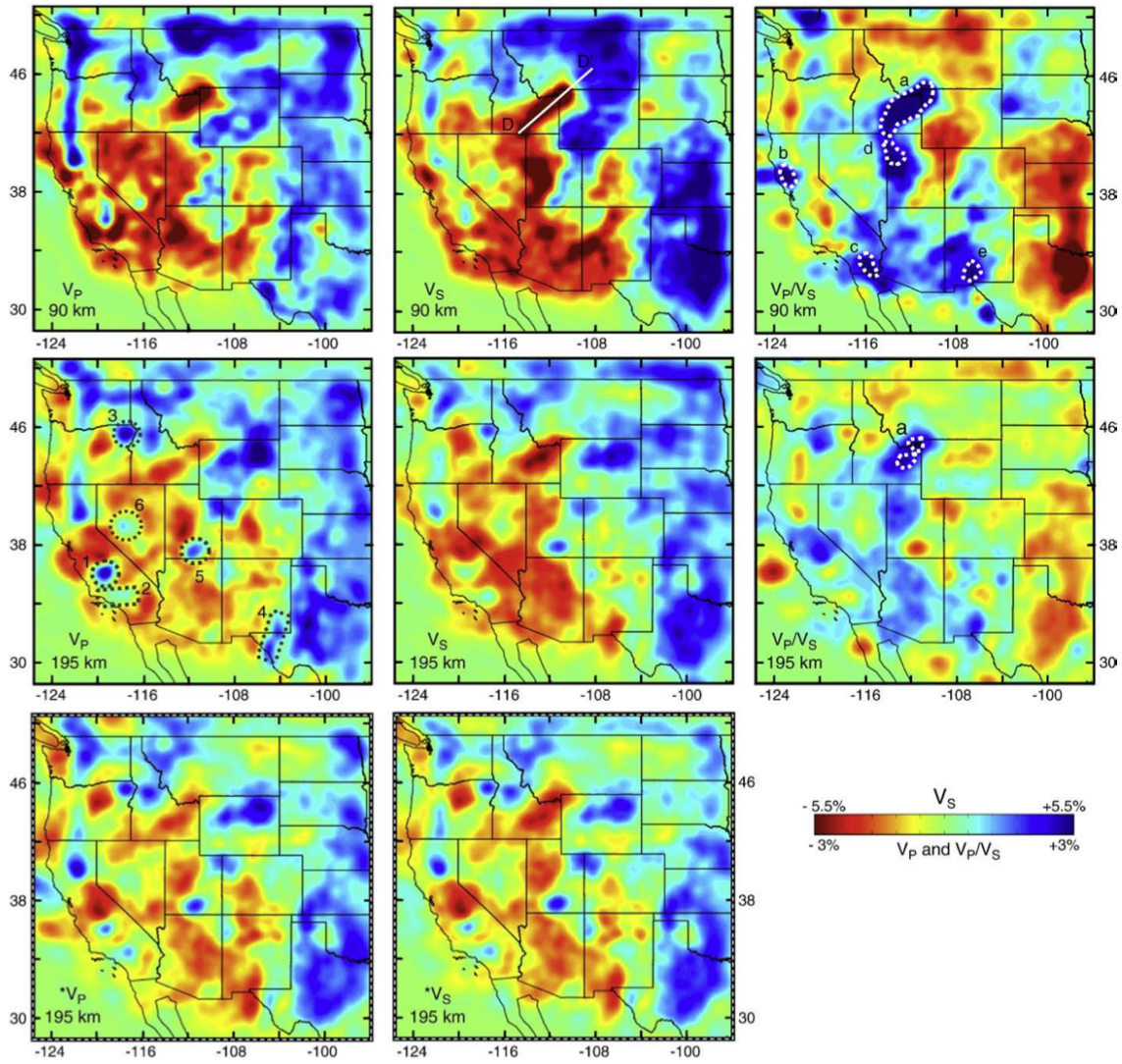

Figure 3.4. Shallow upper mantle map slices. Color represents velocity perturbations relative to the mean in each depth layer and that mean is not constrained by our relative travel-time data. Hypothesized lithospheric instabilities are outlined (gray dashed) on the 195 km V_P map in the left column, second row: (1) southern Great Valley (Zandt et al., 2004), (2) Transverse Ranges (Humphreys and Hager, 1990), (3) Wallowa Mountains (Hales et al., 2005), (4) western Great Plains (Song and Helmberger, 2007), (5) Colorado Plateau (Sine et al., 2008), and (6) central Nevada (West et al., 2009). Inferred partial melt regions (Section 3.2) are outlined (white dashed) on the V_P/V_S maps in the right column. The maximum inferred depth of melt is ~ 195 km beneath (a) Yellowstone and the eastern SRP, and ~ 125 km for (b) the Salton Trough, (c) Clear Lake volcanic field, (d) northeastern Great Basin, and (e) southern RGR.

asthenosphere (Dixon et al., 2004; Yang and Forsyth, 2008) has been suggested, but lateral variations in hydration are unlikely to account for the 5-6% peak-to-peak V_P/V_S variations commonly imaged in the upper 200 km. Jacobsen et al. [2009] find only 0.3% reduction in V_P/V_S for hydrous forsterite with 0.9 wt% H_2O at deep upper mantle pressure (12 GPa), and water solubility is much lower at the depths where the greatest V_P/V_S variations are imaged. There is not consensus as to how strongly melt depletion affects V_P/V_S (Lee, 2003; Schutt and Lesher, 2006). Melt depletion is generally thought to lower V_P/V_S at least slightly, but variations in melt depletion alone cannot account for more than a small fraction of the magnitude of V_P/V_S variations we find in the western U.S. upper mantle. In general, we are lead to conclude that lateral variations in temperature and partial melt are the dominant causes of the imaged structure.

Theoretically, relative δlnVs and δlnVp variations can be diagnostic of the presence of partial melt. As mentioned in section 2.1, $\delta ln V_S/\delta ln V_P$ of 1.6 is predicted for thermal variations, whereas partial melt in the upper mantle is predicted to cause $\delta ln V_S/\delta ln V_P$ values of ~2.2–2.3 (Hammond and Humphreys, 2000). Linear regression of model parameters from the well-sampled portion of the jointly inverted model yields best-fit $\delta ln V_S/\delta ln V_P$ value of 1.8 (Fig. 3.5). This estimate is greater than that derived from the raw residuals, 1.57. We think the difference is a result of integrated sampling of 3-D heterogeneity where the greatest magnitude of $\delta ln V_S/\delta ln V_P$ variations occurs over only a small fraction of the total ray length. We suggest the $\delta ln V_S/\delta ln V_P$ estimate from the joint inversion is too high to be explained solely by thermal variations and the presence of partial melt in the lowest velocity volumes is more consistent with our results.

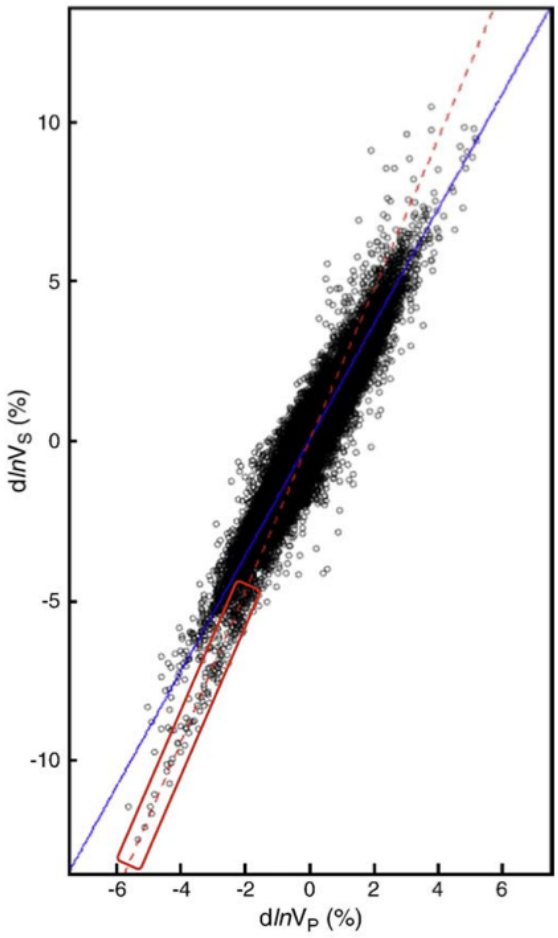

Figure 3.5. Upper mantle $\delta ln V_S / \delta ln V_P$ from the joint inversion. Solid blue line indicates the least-squares fit, 1.8 ± 0.05 (bootstrap standard error). The red dashed line indicates the "partial melt trend" (slope of 2.33). Note that many of the very low-velocity model parameters closely follow the partial melt trend.

Inspection of the scatter plot of $\delta ln V_S$ versus $\delta ln V_P$ model parameters shows that the very low-velocity parameters cluster along two distinct trends rather than being normally distributed about the fit line (Fig. 3.5). The lower trend is approximately the best-fit value, 1.8. The steeper trend is ~2.33, which is approximately the predicted slope for partial melt, and the lowest velocity points follow this trend remarkably closely. We

consider this strong evidence for partial melt in the corresponding mantle volumes. The locations of the model parameters with $\delta \ln V_S < -4\%$ that lie within 0.6% of the $\delta \ln V_S / \delta \ln V_P = 2.33$ "partial melt trend" (but not within 0.3% of the fit line) are outlined on the V_P/V_S tomograms in Figure 3.4.

The greatest concentration of model parameters that follow the partial melt trend underlie Yellowstone and the eastern Snake River Plain (SRP) where the inferred prevalence of partial melt decreases rapidly beneath 160 km and disappears deeper than 195 km. We infer decompression induced partial melting to a depth of 90-125 km beneath the Salton Trough and the Clear Lake volcanic field located at the southern edge of the Juan de Fuca-Gorda (JdF-G) slab. Rollback and sinking of the JdF-G slab is thought to drive toroidal flow of oceanic asthenosphere around the slab edge (Zandt and Humphreys, 2008) with an upward poloidal component to direct asthenosphere into the wedge (Piromallo et al., 2006). Mantle ascent beneath the Salton Trough is driven by oblique plate spreading at the northernmost extension of the East Pacific Rise (Stock and Molnar, 1988). Decompression melting beginning at 90-125 km depth is consistent with hydrated peridotite (300-1000 ppm H_2O) ascending along a ridge adiabat (Hirschmann, 2006), and hydration of the western U.S. mantle is likely after more than 100 My of subduction. A maximum melting depth of 160-195 km beneath Yellowstone is consistent with hydrated peridotite (300-1000 ppm H_2O) ascending along a plume adiabat with an excess temperature of 125-225 K (Hirschmann, 2006). Schutt and Dueker [2008], used modeling of Rayleigh-wave velocities to estimate (at 68% confidence) an excess temperature of ≥120 K beneath Yellowstone, which would be approximately consistent with initiation of melting at 195 km and 1000 ppm H_2O.

More enigmatic are low-velocity model nodes located beneath the northeastern Great Basin and southern New Mexico that also follow the partial melt trend. In the northeastern Great Basin these nodes correlate with a thin crust and seismic lid (Gilbert and Fouch, 2007; Li et al., 2007); thus, decompression melting of a damp asthenosphere is plausible, but difficult to reconcile with relatively sparse young volcanism compared to the previously mentioned locations. In southern New Mexico there is young volcanic activity and modest mantle ascent is expected to accompany slow Rio Grande Rift (RGR) extension, <0.2 mm/yr (Golombek et al., 1983). However, it is only beneath a small segment of the southern RGR that the P and S model parameters follow the partial melt trend while low-velocity nodes beneath the rest of the RGR do not.

Low velocity, high V_P/V_S volumes are generally found beneath young volcanic fields, but aside from the specific locations mentioned above we think the depth extent and magnitude of melting are too small to be clearly identified by our body-wave tomography. We suggest the very low-velocity mantle volumes that follow the partial melt trend require melting over a depth range of at least 1 vertical model node distance (30 km) in the well-sampled volume in order to be imaged. The fact that the $\delta\ln V_S/\delta\ln V_P$ trend of 1.8 for the whole model is steeper than the predicted temperature trend (1.6) suggests that many arrivals to the western U.S. experience some partially molten mantle, most likely over a depth range less than ~30 km thick and shallower than ~60-80 km depth.

Our conclusions regarding upper mantle physical state are generally in agreement with Goes and van der Lee [2002] who suggest that large lateral temperature differences

owing to variable lithospheric thickness can explain most V_P and V_S variations with ~1% melt locally in the most anomalous regions.

3.3. 3-D seismic structure

Seismic heterogeneity is strongly correlated with major tectonic and magmatic features of the western U.S. Prominent long-wavelength features include high-velocity mantle associated with subduction of the JdF-G slab and beneath the relatively undeformed Colorado Plateau and Great Plains, and generally low velocity mantle beneath the transform margin, Basin and Range, SRP, and RGR (Fig. 3.4). Below we discuss salient features of the 3-D V_P, V_S, and V_P/V_S models, and we use knowledge of western U.S. tectonic and magmatic history to make reasoned inferences regarding the geologic origins of anomalous structures.

3.3.1. Evidence for complex subduction

We image a continuous north trending high-velocity slab in the northwestern U.S. upper mantle that must be JdF-G plate subducting beneath the Cascade Arc. The high-velocity slab becomes weak to non-existent beneath northern Oregon at depths greater than ~160 km, whereas the northern and southern portions of the JdF-G slab descend continuously from the trench to depths of ~350 km (Fig. 3.4, 3.6). This defines a slab hole (Roth et al., 2008; Burdick et al., 2008; Tian et al., 2009), which is a robust feature of our P and S tomography models. Assuming a convergence rate of ~4 cm/yr (Gripp and Gordon, 2002), the northern Oregon slab accounts for subduction since only 6-8 Ma, and the segments north and south of the hole account for subduction since ~15 Ma. An abrupt change in subduction geometry at ~15 Ma has also been suggested by geochemical

investigation of back-arc volcanism (Carlson and Hart, 1987). The presence of the hole and the separation of the clearly identified JdF-G slab from deeper high-velocity anomalies indicate a complex subduction history. The strongest case for near-continuous subduction is shown in Figure 3.7 (A-A' and B-B'), but north-south continuity of this feature is variable and nowhere greater than ~500 km. Map-view sections within and beneath the transition zone show a general lack of continuity between slab fragments (Fig. 3.6). Some high-velocity anomalies inferred to be slab fragments beneath the continental interior can be related to western U.S. geologic history. However, a complete accounting of how the large volume of fragmented high-velocity structures relates to the ~5000 km of ocean lithosphere subducted since the Laramide orogeny began (Engebretson et al., 1985) remains a challenge.

A high-velocity "curtain" extends vertically from near the base of the lithosphere to depths of ~250 km beneath Washington and 500-600 km beneath western Idaho (Fig. 3.6, 3.7). Because the overlying crust experienced considerable Eocene extension, including formation of metamorphic core complexes, and voluminous ignimbritic magmatism (Christiansen and Yeats, 1992) it seems unlikely that this area is underlain by thick, intact ancient lithosphere. We suggest a subducted slab origin for the high-velocity curtain, which roughly follows the inferred early Cenozoic Challis subduction zone on the north and east side of the Columbia embayment (Humphreys, 2009). We interpret the curtain to be Farallon slab that was attached to the leading margin of Siletzia when it accreted ~50 Ma. In order for the slab fragment to persist in this location for ~50 Ma it must be of approximately neutral buoyancy. Plate-tectonic reconstructions have young, 5–30 Ma, lithosphere subducting beneath the Pacific Northwest at this time (Madsen et

al., 2006; Mueller et al., 2008), hence initial slab buoyancy would have been nearly neutral. Furthermore, portions of the basaltic crust of this slab may have melted in the shallow mantle potentially contributing to a ~52-45 Ma episode of voluminous magmatism in Idaho and northern Washington (Gaschnig et al., 2009; Madsen et al., 2006) and avoiding the negative buoyancy of an eclogitic ocean crust.

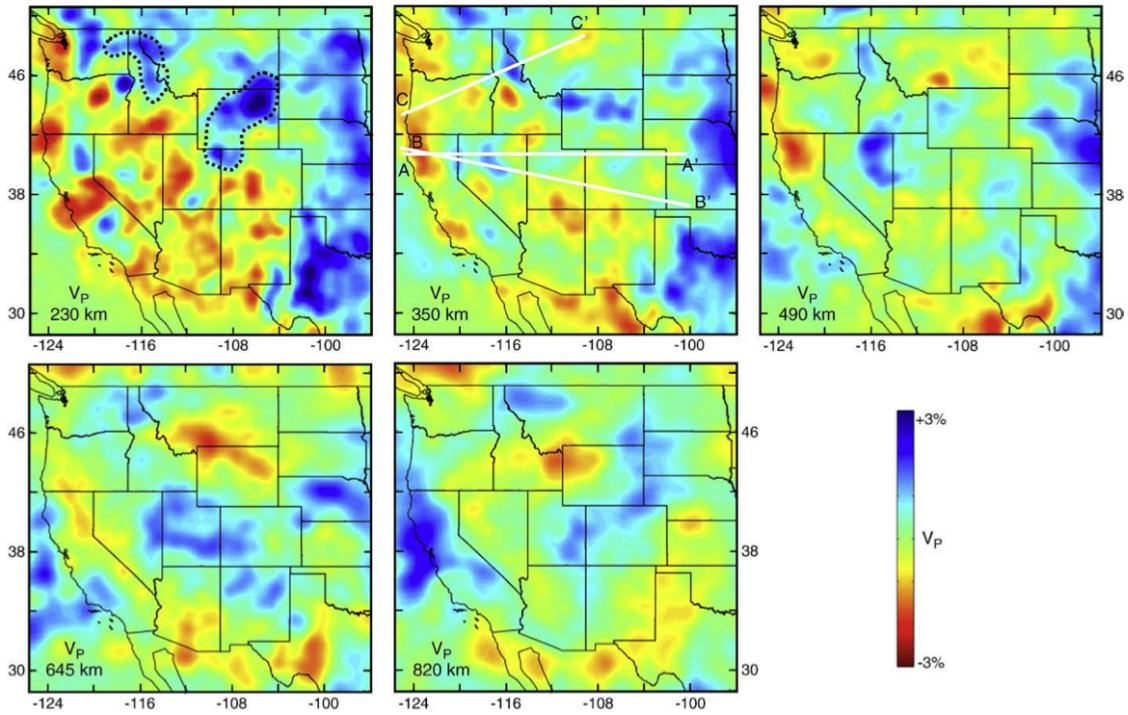

Figure 3.6. Deep upper mantle map slices from the P model. The slab curtain and thick high-velocity lithosphere beneath the Rocky Mountains discussed in Section 3.3.1 are outlined (black dashed) in the upper left panel. The locations of cross-sections A–A′, B–B′, and C–C′ from Fig. 3.7 are indicated.

Regardless of the specific origins of the high-velocity curtain and the hole in the currently subducting JdF-G slab, these structures must fundamentally alter subduction

zone mantle flow. Resulting along-strike variations in asthenospheric flow may contribute to dramatic along-strike changes in Cascade Arc volcanism, with widespread and voluminous volcanism in the Oregon Cascades trending to localized and lower-volume volcanism in northern Washington (e.g., Reiners et al., 2002).

Large high-velocity anomalies trending ~SW-NE are found beneath much of Wyoming, northeast Utah, and northwest Colorado, down to ~250-300 km depth (Fig. 3.6, 3.7). It is difficult to explain how ~1.5 km uplift of this area from near sea level at times prior to the Laramide orogeny (inferred from uplift of Cretaceous marine sediments) can be made consistent with a lithosphere thickness as great or greater than that typically found beneath stable cratons (Lebedev and van der Hilst, 2008). An alternative explanation for this structure is that a buoyant ocean plateau (the Shatsky Rise conjugate) inferred to have subducted during the Laramide orogeny (Livicarri et al., 1981; Saleeby, 2003) stalled beneath this region. Subduction of the plateau beneath North America is thought to have caused slab flattening and erosion of basal lithosphere (Spencer, 1996), which may be partly responsible for the uplift of Wyoming. Transfer of the plateau lithosphere from the subducted Farallon to basal North America lithosphere is compatible with the bight in the Farallon slab imaged in the mid-mantle beneath Hudson Bay (Bunge and Grand, 2000). Furthermore, the presence of lateral buoyancy variations in the Farallon slab offers a mechanical explanation for the dissected geometry of the inferred Laramide-age subducted slab and the chaotic distribution of volcanism thought to represent slab flattening (Coney and Reynolds, 1977) and subsequent removal beneath the Rocky Mountains. In order for basal accretion of ocean plateau lithosphere to cause a significant net increase in buoyancy most of its basaltic crust must have been

mechanically removed as it traversed the base of the North America lithosphere. If the thick basaltic crust remained entirely intact this explanation for the anomaly does not seem viable because we expect the basalt to convert to dense eclogite.

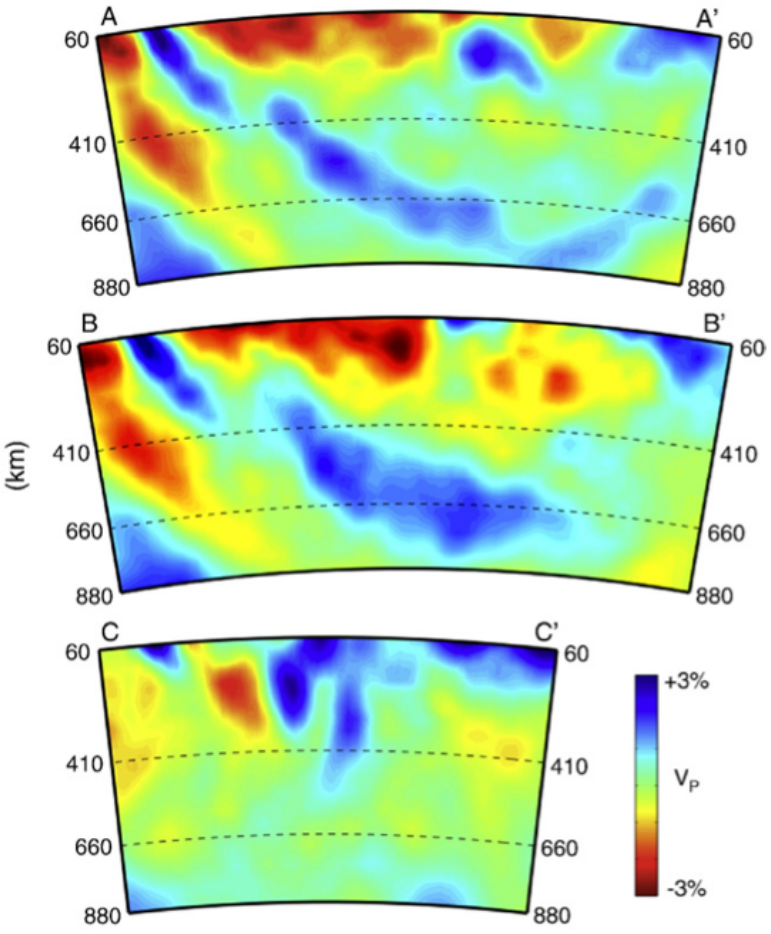

Figure 3.7. Cross-sections from the P model. The locations of A–A′, B–B′, and C–C′ are shown the map slices in Fig. 3.6. Section C–C′ crosses the slab hole and slab curtain discussed in Section 3.3.1.

A strongly anomalous high-velocity body so great in volume that it must be subducted ocean lithosphere extends from ~300 km depth beneath Nevada to ~800 km depth beneath Utah and Colorado (Fig. 3.6, 3.7). Large high-velocity anomalies are also found at 600-900 km depth beneath eastern Wyoming and the Great Plains and are inferred to be subducted slab fragments (Fig. 3.6). The dismembered structure of these high-velocity anomalies is intriguing considering the rather simple coherent east-dipping structure of the older Farallon slab in the mid-mantle beneath the eastern U.S. (Bunge and Grand, 2000). Plate reconstruction models predict that the highly fragmented slab lies beneath paleo-subduction zones as old as ~75 Ma (Lithgow-Bertelloni and Richards, 1998), i.e., near the beginning of the Laramide orogeny. From these results, we infer patchy and incomplete removal of flat subducting Laramide slab accompanied by slab tearing associated with Eocene accretion in the northwestern U.S., rather than coherent post-Laramide rollback.

3.3.2. Lithospheric heterogeneity and instabilities

We find more complex structure within and near the base of the lithosphere (60-160 km) than continental (Bedle and van der Lee, 2009) or global (Lebedev and van der Hilst, 2008) scale studies find using longer-period data from sparser networks that pre-date the TA. The most prominent difference in regional lithospheric structure is a southwest trending swath of high-velocity lithosphere extending from the central Colorado Plateau to northeastern Wyoming, with generally lower-velocity mantle beneath the adjacent SRP, Basin and Range, Colorado Rockies, and RGR (Fig. 3.4). This arm of high-velocity lithosphere crosses the continental divide in WY and underlies some

of the highest topography in the western U.S. A smaller region of high-velocity lithosphere lies beneath western Idaho and easternmost Oregon and Washington, straddling the boundary between Precambrian continental lithosphere and the accreted oceanic terranes (Fig. 3.4). In the tectonically stable portion of the western U.S., high-velocity mantle underlies northern Montana and the western Great Plains south of Nebraska. Thus, strong mantle heterogeneity is being revealed beneath both tectonically active and tectonically quiescent domains of the western U.S.

Most of the Colorado Plateau is distinguished from the surrounding Basin and Range and RGR provinces by the presence of laterally continuous high-velocity mantle from 60–125 km depth (Fig. 3.4), and the Colorado Plateau-Great Basin transition is one of the strongest upper mantle velocity gradients in the western U.S. (Sine et al., 2008), we find up to 8% V_P and 14.5% V_S variations over <150 km. At these depths, however, the transition from Colorado Plateau to Basin and Range mantle often lies inboard of the Colorado Plateau margin. This is especially true of the southwestern plateau (including the Grand Canyon and San Francisco Peaks volcanic field). In addition, isolated, high-velocity volumes beneath southern Utah and northwestern New Mexico extend to depths of ~230 km and ~200 km, respectively (Fig. 3.4). Low seismic velocities beneath the margins of the Colorado Plateau, in conjunction with the elevated plateau rim and co-located geoid high (Karlstrom et al., 2008), frequent seismicity, and late-Cenozoic migration of volcanism onto the Colorado Plateau, suggest approximately concentric thermal erosion of a lithospheric step originally located beneath the topographic boundary of the Colorado Plateau (Karlstrom et al., 2008; Roy et al., 2009). The presence of the two deeper, drip-like high-velocity bodies and the absence of thick high-velocity

mantle lithosphere beneath much of the southwestern Colorado Plateau indicate that more localized 3-D lithospheric downwelling also is occurring, which may contribute importantly to the Cenozoic uplift of the plateau.

In several other areas, small-scale (100-200 km) high-velocity features extend to depths of 200-250 km, and often are surrounded by low-velocity, high V_P/V_S mantle (Fig. 3.4). The large magnitude and drip-like geometry of these anomalies lead us to infer that both 3-D gravitational instabilities and edge driven convection are actively modifying the western U.S. lithosphere. Temperature contrast owing to lithospheric downwelling probably is the dominant cause of these anomalies. However, imaged large velocity reductions (with respect to the already low-velocity mean of western U.S. asthenosphere) and the expectation of ascending return flow suggest that partial melt may be present within the very low-velocity volumes. Small-scale upper mantle convection driven by the recent sinking of dense mafic roots of plutons has been proposed for the uplifted southern Sierra Nevada (Ducea and Saleeby, 1998; Zandt et al., 2004) and Wallowa Mountains (Hales et al., 2005), and oblique convergence at the "Big Bend" in the San Andreas fault is thought to drive downwelling of mantle lithosphere creating the high-velocity anomaly beneath the Transverse Ranges (Bird and Rosenstock, 1984; Humphreys and Hager, 1990). Edge convection driven by abrupt changes in lithospheric thickness has been proposed to explain mantle velocity contrasts at the edge of the Colorado plateau (Sine et al., 2008) and beneath the Rio Grande Rift-Great Plains transition (Gao et al., 2004; Song and Helmberger, 2007).

3.3.3. Snake River Plain-Yellowstone hotspot

The most prominent low-velocity, high V_P/V_S anomaly occupies the ~200 km beneath Yellowstone and the eastern SRP (Fig. 3.4, 3.8). A broader, lower magnitude low-velocity, high V_P/V_S anomaly occupies the transition zone and extends to ~900 km beneath the Yellowstone region. It appears separate from the shallow anomaly in the V_P model and weakly connected in the V_S and V_P/V_S models (Fig. 3.8). The deeper low-velocity volume extends just to the bottom of what we consider the well-resolved model domain (885 km). It is worth noting that the anomaly is not present in the bottom two layers of the entire model. If a low-velocity conduit extended to greater depth than the base of our model (1015 km), we would expect a large velocity anomaly to accumulate in the deepest layers. In agreement with other recent studies (Yuan and Dueker, 2005; Sigloch et al., 2008; Burdick et al., 2009; Tian et al., 2009; Smith et al., 2009, Xue and Allen, 2010), we do not find a strong low-velocity conduit that extends continuously into the lower mantle. The proximity of major high-velocity bodies suggests mantle ascent beneath Yellowstone is driven by sinking cool masses as well as its own positive buoyancy (Fig. 3.6). The ~12 m geoid high centered on Yellowstone indicates that the Yellowstone topographic swell is compensated at depths greater than the rest of elevated western U.S. (Lowry et al., 2000), which is attributed to buoyancy of the very low velocity mantle imaged in the upper 200 km.

4. Conclusions

We provide a new level of constraint on 3-D seismic heterogeneity and the distribution of partial melt in the western U.S. upper mantle. The seismic structure

presented here and the spatial and temporal distribution of volcanic and tectonic activity in the western U.S. indicate a complex syn- and post-Laramide subduction history and

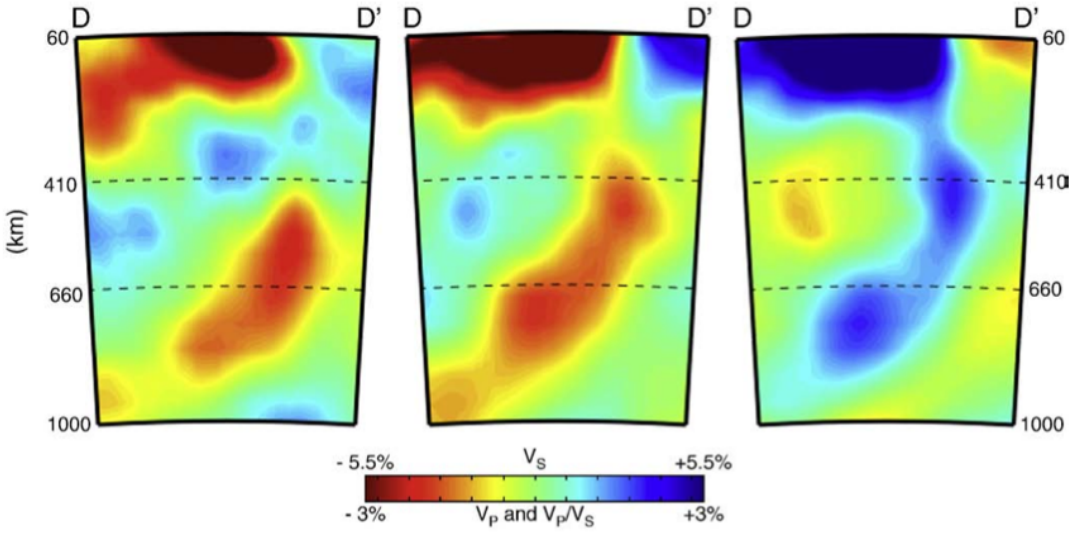

Figure 3.8. Cross-section through the eastern SRP and Yellowstone. The location of the cross-section D–D′ is labeled in Fig. 4. All panels show the same section. Isolated Vp model (left), isolated Vs model (center), and Vp/Vs model from the joint inversion (right). Maximum perturbations are −4.75% Vp, −11% VS, and +7% Vp/Vs at 60–90 km depth beneath Yellowstone and the easternmost SRP.

currently active widespread small-scale convection. It remains a challenge to understand specifically all the events that lead to segmentation subducted Farallon slab and how those events relate to surface geologic activity. At present, a diverse range of small-scale convective processes appear to be active beneath the western U.S. including 3-D lithospheric drips, edge-driven convection, and an upper mantle plume, but further constraints on upper mantle physical state are necessary to determine the conditions that

drive this spectrum of activity. Additionally, it is unclear how the provincially heterogeneous lithosphere we image supports the elevation of the western U.S. plateau, and we place particular emphasis on a need to understand the buoyancy structure of the high-velocity lithosphere that apparently underlies much of the high topography of Wyoming and the Colorado Plateau. Progress in these directions will require knowledge of 3-D attenuation structure and careful integration of body-waves, surface-waves, and receiver functions to achieve shorter wavelength resolution of mantle structure.

This chapter presents images of mantle velocity structure beneath the entire western U.S. and discusses the broad implications of the images for mantle physical state and convective processes. A hypothesized relict slab imaged beneath the interior of the northwest U.S. motivates re-evaluation of Cenozoic evolution of the northwest U.S. convergent margin in the following chapter.

CHAPTER IV

SEISMICALLY IMAGED RELICT SLAB FROM 55 MA SILETZIA ACCRETION TO NORTHWEST U.S.A.

This work was published in volume 39 of Geology in February, 2011. Coauthor Eugene Humphreys provided guidance in the analysis, intepretation, and editorial process. I performed all analysis and was the primary author of the manuscript.

1. Introduction

New western U.S. seismic images enabled by EarthScope's USArray provide for the first time information on upper mantle structure over a large area of continent with high resolution. In this paper we discuss the Pacific Northwest (PNW) portion of our recent tomographic models (Schmandt and Humphreys, 2010a) to focus on a prominent but previously unresolved "curtain" of high-velocity mantle extending vertically from beneath central Idaho to near the eastern edge of the Cascades in northern Washington and extending down to depths of 230-600 km (Figs. 1 and 2). The only plausible explanation for this large volume of high-velocity mantle is recently subducted ocean lithosphere. We address below the seismic, tectonic, and magmatic evidence that this structure is subducted Farallon slab abandoned in the upper mantle during the ~55 Ma accretion of Siletzia, which we define as the fragment of Farallon lithosphere that filled the Columbia Embayment (CE) in the Eocene. We then proceed to consider the seismic and geodynamic plausibility that ocean lithosphere subducted in the early Cenozoic did

not lose its seismic contrast or sink into the Earth. Finally, we consider the implications of this structure for early Cenozoic evolution of the western U.S. convergent margin.

2. Pacific Northwest Tomography

We create high-resolution P-wave and S-wave images of the upper mantle beneath the western U.S. by inverting 248,000 P and 84,000 S relative travel-time residuals of teleseismic earthquakes observed by USArray and more than 1700 additional stations (Schmandt and Humphreys, 2010a). The inversion uses recent advances in western U.S. crust models (Yang et al., 2008; Gilbert and Flesch, 2009) to better isolate the mantle component of residual times and 3-D frequency-dependent sensitivity kernels to map residuals (measured in multiple frequency bands) into velocity structure. Horizontal node spacing is 40 km within the footprint of the USArray, and vertical node spacing increases gradually with depth from 30 km at 60-90 km depth, to 65 km at >820 km depth. Schmandt and Humphreys (2010b) describe the method in detail. Resolution tests demonstrate excellent recovery of upper mantle structures with length scales ≥70 km, with typical peak amplitude recovery of 70-80% for V_P and 60-70% for V_S. V_P resolution is slightly better than V_S resolution in the PNW as a result of 150 additional short period stations (Fig. 4.1), a greater number of high-quality teleseismic P arrivals, and shorter wavelength sampling of teleseismic P arrivals.

Figures 4.1 and 4.2 show three distinctive high-velocity structures beneath the PNW. A prominent, relatively small and approximately elliptical body is imaged below the

source area of the Columbia River flood basalts in the Wallowa Mountains of northeast Oregon. This structure may owe its creation to basalt depletion or lithospheric

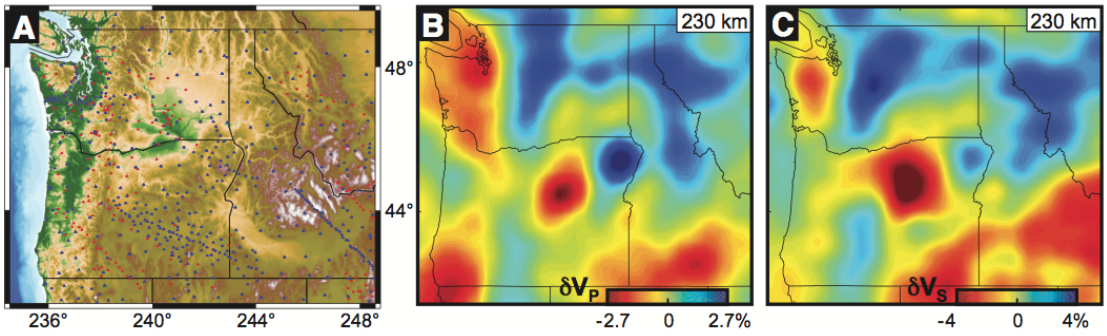

Figure 4.1. Regional topography and station map. A) Regional topography and stations used in our study. Blue indicates stations used for P and S data; red indicates short-period stations used only for P data. Backarc area underlain by Siletzia is well approximated by low-lying Columbia basin (see Fig. 4.2). B) P-wave velocity variations. C) S-wave velocity variations.

delamination (Hales et al., 2005). A second high-velocity feature is the slab-like structure beneath the Cascade arc, which must be the steeply dipping subducted Juan de Fuca slab. The subject of this paper is the high-velocity curtain extending vertically from the base of North America lithosphere to depths of ~230 km beneath eastern Washington and 450-600 km beneath northern Idaho and westernmost Montana (Figs. 4.1 and 4.2). Several recent tomography studies using USArray data find a large volume of vertically elongated high-velocity mantle in this region (e.g., Roth et al., 2008; Sigloch et al., 2008; Burdick et al., 2009; Tian et al., 2009; Xue and Allen, 2010), although not as a feature distinct from the smaller anomaly beneath northeast Oregon. Our better resolution in this area is a result of data from 30 stations in the Wallowa Mountains flex-array experiment. Based on the excellent recovery of input structure in synthetic tests we consider the high-velocity curtain and its separation from the Wallowa Mountains high-velocity anomaly to

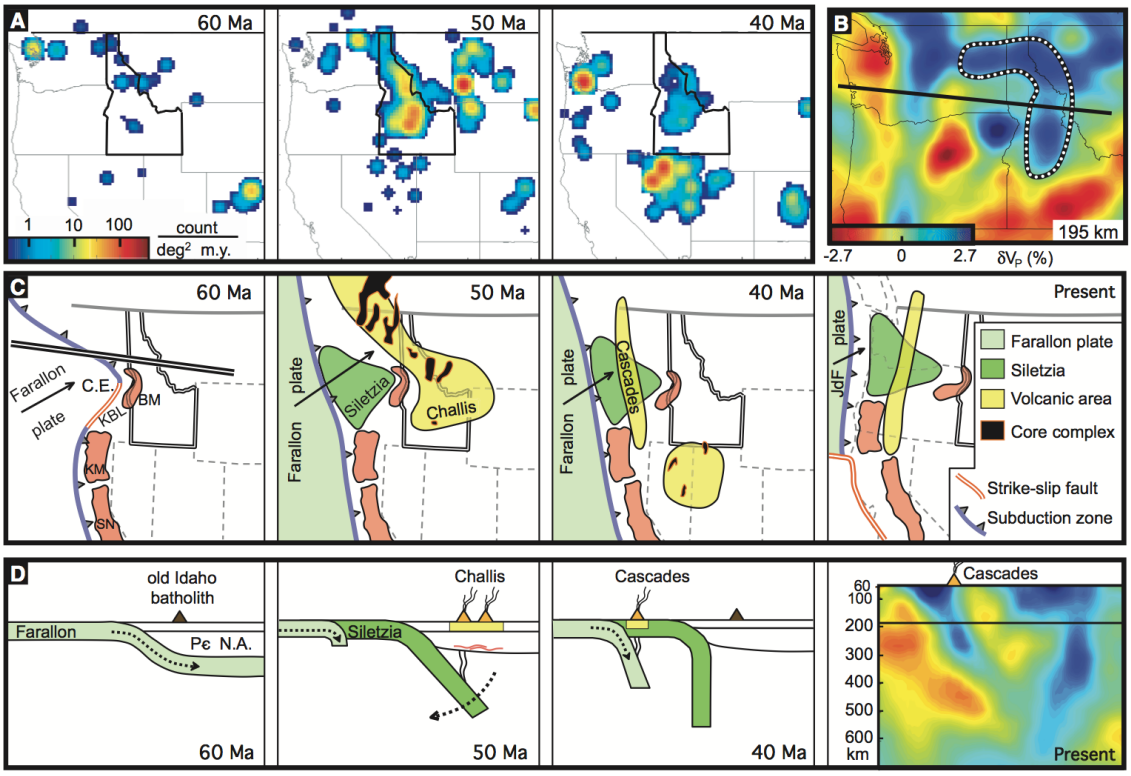

Figure 4.2. Maps and cross sections of northwestern U.S. at 60, 50, 40, and 0 Ma. Border of Idaho is highlighted. A: Maps show- ing density of reported dated igneous rocks from NAVDAT (North American volcanic and intrusive rock database; Walker et al., 2004). Data are binned in time and space (age data distributed equally over reported range, and age uncertainty >10 m.y. rejected). Results are smoothed over 50 km in space and 1 m.y. in time. B: P-wave tomography, emphasizing correlation between imaged curtain and Challis magmatism. Dotted line—Siletzia curtain outline. Dark line location of cross-section A–A′. C: Maps illustrating regional tectonic and magmatic evolution, modified after Dickinson (2006). Intact and coherent units defined by presence of Mesozoic to Cretaceous plutons and associated arc-related rocks are shown in pink; Klamath Mountains (KM), Blue Mountains (BM), and Sierra Nevada (SN). Prior to accretion, 60 Ma, Klamath–Blue Mountains lineament (KBL) is shown as transform boundary (Riddihough et al., 1986). At 60 Ma Farallon plate subducted to northeast in Columbia Embayment (C.E.). Siletzia accreted and subduction stepped west ca. 55–53 Ma, and by 50 Ma Challis magmatism was strong (JdF—Juan de Fuca). D: Cross sections (along B–B′ shown in C, left panel) show our interpretation of subduction history. At 60 Ma, Farallon slab subducts flat against Precambrian (Pc) North America (N.A.). Then, shortly after Siletzia accretion (50 Ma), Cascadia subduction initiates and abandoned, previously flat Farallon slab rolls back, exposing basal North America and Farallon crust to inflowing asthenosphere, causing melting. Event is over by 40 Ma, and little has changed to present, represented by tomography cross section, A–A′.

be robust features. The maximum depth of the curtain being in the transition zone beneath northern Idaho is supported by receiver function results indicating a spatially correlated upward deflection of the 410 km discontinuity and no strong deflection of the 660 (Eagar et al., 2010).

3. Volcanic and Tectonic Context

Prior to the Laramide orogeny, subduction of Farallon ocean lithosphere beneath western North America generated arc magmatism along the entire plate margin. In the PNW of the U.S. magmatism was concentrated in the Idaho batholith (Giorgis et al., 2005), with this inboard setting related to subduction beneath the northeast margin of the CE (Fig. 4.2c). Starting ~80 Ma, magmatism in the Idaho batholith lost most of its mantle geochemical signature and became increasingly lower crustal in composition and decreasingly active, finally becoming amagmatic at 54 Ma (Fig. 2a; Gaschnig et al., 2009). This commonly is attributed to Farallon slab flattening against the base of North America (Feeley, 2003), similar to accountings for Laramide-age magmatic quiescence to the south (Coney and Reynolds, 1977). The magmatic lull was accompanied by Laramide thrusting in the Rocky Mountains of Canada and the U.S., with thrusting continuing to ~53 Ma in Montana (van der Pluijm et al., 2006). The Laramide-style episode was followed by an intense magmatic flare-up, starting ~55 Ma in southern British Columbia (Geherels et al., 2009) and ~52 Ma in the U.S. (Gaschnig et al., 2009), with the initiation of compositionally and isotopically diverse (Madsen et al., 2006) Challis-trend magmatism and associated core-complex extension (Foster et al., 2007). Siletzia ocean lithosphere accreted to North America within the CE about this time, necessitating

initiation of Cascadia subduction on the west side of Siletzia (Fig. 4.2c) (Wells et al., 1984).

The sudden onset of intense, geochemically diverse and relatively alkalic magmas, including adakites, led Breitsprecher (2003) and Madsen et al. (2006) to attribute this volcanic activity to asthenospheric upwelling through a Kula-Farallon slab window, incorporating slab crust in the process. As discussed below, we attribute this magmatism to asthenospheric upwelling as the flat-subducting Farallon slab fell away from the base of North America (Feeley, 2003; Coney and Reynolds, 1977; Humphreys, 2009). This phase of magmatism ended in British Columbia ~48 Ma (Gehrels et al., 2009) and Challis magmatism waned 48-45 Ma (Gaschnig et al., 2009) as magmatism swept west across Oregon (the Clarno volcanics, ~45-40 Ma, Retallack et al., 2000) and the Cascade arc initiated ~45-40 Ma (Fig. 4.2a; Christiansen and Yeats, 1992). Initiation of Cascade magmatism was a response to accretion of Siletzia and outward stepping of subduction.

This geologic record supports a history in which Farallon ocean lithosphere subducted flat against North America during the Laramide orogeny and fell away shortly after Siletzia accretion, at the time of Challis-trend magmatism. We suggest that the imaged curtain is the Farallon slab that fell away from basal North America ~50 Ma, still present beneath an area roughly coincident with the Challis-trend magmatism. The seismic and dynamic viability of the high-velocity "curtain" being subducted ocean lithosphere stalled in the upper mantle since ~50 Ma is addressed next.

4. Physical Origin of the Siletzia Curtain

Seismically fast upper mantle may be attributed to subducted ocean lithosphere, thick continental lithosphere or small-scale convective downwelling or delamination of continental lithosphere (Bird, 1979). The imaged high-velocity curtain extends below a belt of Cretaceous plutons and Cenozoic core complexes, where lithosphere is expected to be thin, and convective removal of basal lithosphere could not create an anomalous volume as large as that imaged. We infer that the imaged curtain must be subducted ocean lithosphere – an idea supported by its slab-like form and location near where the last subducted slab would have been in this area.

We calculate the seismic structure expected for stalled ocean lithosphere to assess the plausibility of this idea. The age of Farallon plate upon subduction in the CE is ≤55 m.y. (Muller et al., 2008). Using the thermal parameters of van Keken et al. (2002), we represent a reasonable range of possibilities by calculating the thermal structure for ocean lithosphere of two ages (20 and 50 m.y.) and then letting these evolve conductively within an asthenosphere for 50 m.y. The older slab is 350ºC cooler than the asthenosphere across its core (of 50 km width) and has a width of 180 km (at temperatures 50ºC cooler than asthenosphere); the younger slab is 250ºC cooler than asthenosphere and has a width of 160 km. Assuming mean upper mantle Q_S=100 (Dalton et al., 2008) and no bulk attenuation, these core temperatures predict core seismic anomalies δV_P = 2.3-3.3% and δV_S = 3.8-5.3% (Karato, 1993). For structures 150-200 km wide, our P and S models recover ~80% and ~70% of the actual amplitudes. Hence, we expect the thermal anomaly of our modeled slabs would be imaged as seismic anomalies

of δV_P = 1.8-2.6% and δV_S = 2.7-3.7%. This compares well with our observed core seismic anomalies of δV_P = 1.5-2.5% and δV_S = 2.5-4.0%.

Other factors contributing to the expected seismic contrast of the slab with the asthenosphere include effects caused by dehydration upon formation of lithosphere at the spreading center and seismic anisotropy, although we have little knowledge about the actual state of either of these properties. For the effects of water, if we assume a 50 km thickness of dehydrated slab to be seismically faster by an amount equivalent to temperature decrease of 100ºC (Karato, 2003), it can increase the expected imaged velocities by δV_P = 0.6% and δV_S = 1.0%. If we assume ocean lithosphere anisotropy is preserved upon subduction, we would expect teleseismic P and S waves to be advanced in the steeply dipping Siletzia curtain, compared to arrivals that traverse the asthenosphere. Using average ocean lithosphere anisotropy (Kustowski et al., 2008), δV_P = 4.6% and δV_S = 2.4% compared to an isotropic mantle, and knowing that the mantle away from the Siletzia curtain creates 0.5-2.5s SKS splits (Long et al., 2009), the velocity anomalies could, in principal, be even larger. We conclude that the seismic magnitude of the Siletzia curtain is well within the range of expected values for slab that stalled ~50 m.y. ago.

If the imaged curtain is stalled ocean lithosphere, any of its crust that was not mechanically under-accreted to North America during flat-slab subduction would warm quickly after stalling and melt. The loss of what would have become an eclogitic crust would have eliminated most of the slab's negative buoyancy (Cloos, 1993), helping to explain why the slab has not sunk. Melting of either under-accreted ocean crust or still-attached slab crust is consistent with the vigor and diversity of Challis-trend magmatism,

including the eruption of magmas that have been attributed to the melting of ocean-lithosphere crust (e.g., Madsen et al., 2006).

The vertical orientation of the curtain 50 m.y. after it stalled in the upper mantle can potentially be explained by its location near the transition from westward flow of asthenosphere into the mantle wedge beneath Oregon and Washington to east-northeastward flow of asthenosphere beneath the continental interior (Humphreys et al., 2000).

5. Discussion

We propose a model for Siletzia accretion (Fig. 4.2d) that is consistent with both PNW tectonic and magmatic history and our tomography. The explanation prior to our upper mantle imaging invoked end-on subduction of the Kula-Farallon spreading center, creating a slab window that caused asthenospheric upwelling and melting of slab crust (Breitsprecher et al., 2003). This model appears inconsistent with the location of the imaged mantle curtain and it does not account for the preceding magmatic lull. We propose an alternative history that involves rollback of flat-subducting Farallon slab following Siletzia accretion, which ascribes magmatism to asthenospheric flow into the opening mantle wedge and to melting of the stalled Farallon slab crust, either as the top of the slab or as a unit transferred to the base of North America during flat subduction. Pre-accretion magmatic quiescence and the thrusting of basement-cored uplifts in Montana prior to ~53 Ma are attributed to flat-subduction. Rapid ~53 Ma initiation of vigorous magmatism and extension is attributed to a rollback-like foundering of ocean lithosphere (Feeley, 2003), and we infer that accretion of Farallon ocean lithosphere, Siletzia, within the CE occured shortly before slab foundering, ~55 Ma. In this context,

Challis-trend magmatism is thought to result from asthenospheric inflow, decompression melting and heating the hydrated base of North America lithosphere likely accompanied by melting of stalled Farallon slab crust. Sudden initiation of core complexes is attributed to gravitational collapse of a pre-existing crustal welt (Coney and Harms, 1984), enabled by cessation of the compression created by flat subduction and seamount collision, and by subduction initiation at Cascadia (Fig. 4.2c) creating extensional stresses (Gurnis, 1992). The modern PNW tectonic configuration was largely established by 40 Ma (Fig. 4.2d).

Siletzia accretion and creation of a normal-dip subduction zone at Cascadia must have torn the PNW slab to separate it from the adjacent southern portion of flat-subducting slab responsible the continued quiescence of arc volcanism in the Sierra Nevada and the ongoing Laramide orogeny. Following accretion, the ignimbrite flare-up propagated north to south across the Great Basin (~45-21 Ma) (Fig. 4.2c), which we attribute to north-to-south retreat of the northern margin of the flat slab (Humphreys, 1995). Hence, Siletzia accretion appears to trigger the northern sweep of the ignimbrite flare-up and perhaps the end of the Laramide orogeny. Abandonment of ocean lithosphere beneath continental margins during subduction termination may not be a rare occurrence as recent Rayleigh wave tomography studies find a subducted slab fragment beneath Baja California (Zhang et al., 2009; Wang et al., 2009). If not unusual, events such as these may be important for understanding diversity in convergent margin volcanism and the fate of subducted slabs.

CHAPTER V

CONCLUSIONS

This dissertation presents a new seismic tomography method, application of that method to P-wave and S-wave data from a large-aperture seismic array of unprecedented density, and uses the resulting images of mantle structure in conjunction with constraints on western U.S. geologic history to make new inferences regarding the Cenozoic evolution of the western U.S. Cordillera and mantle contributions to present-day magmatic activity and elevation.

The seismic structure of the southern California upper mantle presented in Chapter II is strongly heterogeneous and the magnitude of seismic velocity variations is greatest in the upper 150-200 km. Improved resolution confirms the presence and basic geometry of the Transverse Ranges high-velocity anomaly and suggests lateral thinning of the anomaly beneath the trace of the San Andreas fault. The Isabella anomaly beneath the southern Great Valley is shown to be even larger than that previously imaged using less data. This large volume and lack of a strong gravity anomaly are difficult to reconcile with its origin being entirely attributed to a delaminated mafic cumulate root of the Sierra Nevada batholith. The depth extent of low-velocity and high V_P/V_S mantle associated with oblique extension in Salton Trough suggests significant volatile content in the regional upper mantle.

Tomography of the entire western U.S. mantle to a depth of 1000 km is presented in Chapter III. The geometry and amplitude of V_P, V_S, and V_P/V_S variations in the upper 200 km of the mantle suggests a provincially heterogeneous lithosphere and the

occurrence of widespread small-scale convection beneath the Cordilleran interior. Partially molten mantle is inferred beneath Yellowstone and the eastern Snake River Plain (SRP), the Salton Trough, and the Clear Lake volcanic field. The inferred depth extent of partial melt is consistent with a generally hydrated upper mantle and elevated temperatures beneath the eastern SRP and Yellowstone. Despite continuous subduction since the Cretaceous, the distribution of sub-lithospheric high-velocity anomalies is dissected. Based on the new tomography models, western U.S. geologic history, and plate–tectonic reconstructions, I infer patchy and incomplete removal of the flat-subducting Laramide slab.

Chapter IV presents a Cenozoic tectonic synthesis for the Pacific Northwest, which is motivated by tomography images of a large high-velocity "curtain" extending vertically beneath the ca. 50 Ma Challis magmatic trend to maximum depths of 230–600 km. I interpret this structure as subducted Farallon ocean lithosphere that stalled with the ca. 55 Ma accretion of the Siletzia microplate to North America within the Columbia Embayment, and consider the regional tectonic implications. The abrupt switch ca. 53 Ma from Laramide thrusting and magmatic quiescence to extension and vigorous magmatism in the northwestern United States is evidence for foundering of the flat-subducting Farallon slab. To account for the imaged curtain, foundering apparently occurred by rollback after Siletzia accretion terminated subduction within the Columbia Embayment. After Siletzia accretion, normal dip Cascadia subduction initiated west of Siletzia, evidenced by arc volcanism in Oregon and Washington beginning ca. 45-40 Ma, while continued quiescence of the Sierra Nevada arc suggests persistence of flat subduction to the south. Kinematically, this requires a tear in the subducted Farallon slab near the

latitude of southern Oregon. I propose that north to south propagation of this torn slab edge propagated the ignimbrite flare-up across what now is the northern Basin and Range and ended the Laramide orogeny.

REFERENCES CITED

Chapter II

Anderson, O. L., Isaak, D., Oda, H. (1992). High-temperature elastic constant data on minerals relevant to geophysics. Reviews of Geophysics, 30, 57-90.

Atwater, T. (1970). Implications of plate tectonics for Cenozoic tectonic evolution of western North America. Geological Society of America Bulletin, 81, 3513–3536.

Becker, T. W. & O'Connell, R. J. (2001). Predicting plate velocities with mantle circulation models, Geochemistry, Geophysics, Geosystems. 2, doi:10.1029/2001GC000171.

Benz, H. M., Zandt, G., Oppenheimer, D. H. (1992). Lithospheric Structure of Northern California From Teleseismic Images of the Upper Mantle. Journal of Geophysical Research. 97, 4791–4807.

Biasi, G. P. & Humphreys, E. D. (1992). P-wave image of the upper mantle structure of central California and southern Nevada, Geophysical Research Letters. 19, 1161-1164.

Bird, P. & Rosenstock, R. W. (1984). Kinematics of present crust and mantle flow in southern California, Geological Society of America Bulletin. 95, 946–957.

Boyd, O. S., Jones, C. H., Sheehan, A. F. (2004). Foundering lithosphere imaged beneath the southern Sierra Nevada, California, USA. Science. 305, 660-662.

Bulau, J. R., Waff, H. S., Tyburczy, J. A. (1979). Mechanical and thermodynamic constraints on fluid distribution in partial melts, Journal of Geophysical Research. 84, 6102-6108.

Christiansen, R.L. & Yeats, R.S. (1992). Post-Laramide geology of the Cordilleran region: The Cordilleran Orogen, Conterminous U.S. The Geology of North America, 3, 261–406.

Crowe, B., Self, M., Vanlman, D., Amos, R., Perry, F. (1983). Aspects of potential disruption of a high-level nuclear waste repository in southern Nevada. Journal of Geology. 91, 259-276.

Dahlen, F. A., Hung, S.-H., Nolet, G. (2000). Frechet kernels for finite-frequency traveltimes, I. Theory. Geophysical Journal International. 141, 157–174.

Engebretsen, D. C., Cox, A., Gordon, R. G. (1985). Relative motions between oceanic and continental plates in the Pacific Basin. Geological Society of America Special Paper. 206, 560–569.

Faul, U.H., Toomey, D.R. & Waff, H.S. (1994). Intergranular basaltic melt is distributed in thin, elongated inclusions, Geophysical Research Letters. 21, 29-32.

Fay, N. P., R. A. Bennett, J. C. Spinler, and E. D. Humphreys (2008). Small-scale upper mantle convection and crustal dynamics in southern California. Geochemistry, Geophysics, Geosystems. 9, Q08006, doi:10.1029/2008GC001988.

Goes, S., Govers, R., Vacher, P. (2000). Shallow mantle temperatures under Europe from P and S wave tomography, Journal of Geophysical Research. 105, 11,153 – 11,170.

Grand, S. P. & Helmberger, D. V. (1984). Upper mantle shear structure of North America. Geophysical Journal of the Royal Society. 76, 399–438.

Hadley, D. M., and H. Kanamori (1977). Seismic structure of the Trans- verse Ranges, California, Geol. Soc. Am. Bull., 88, 1461–1478.

Hales, A. L., and H. A. Doyle (1967) P and S travel-time anomalies and their interpretation, Geophys. J. R. Astron. Soc., 13, 403-415.

Hammond, W. C. & Humphreys, E. D. (2000). Upper mantle seismic wave velocity: Effects of realistic partial melt geometries. Journal of Geophysical Research. 105, 975–986.

Humphreys, E. D., Clayton, R. W., Hager, B. H. (1984). A tomographic image of mantle structure beneath southern California. Geophysical Research Letters. 11, 625–627.

Humphreys, E. D. & Clayton, R. W. (1990). Tomographic image of the southern California mantle. Journal of Geophysical Research. 95, 19,725–19,746.

Humphreys, E. D. & Hager, B. H. (1990). A kinematic model for the late Cenozoic development of southern California crust and upper mantle, Journal of Geophysical Research. 95, 19,747–19,762.

Hung, S.-H., Dahlen, F. A., Nolet, G. (2000). Frechet kernels for finite frequency traveltimes—II. Examples. Geophysical Journal International. 141, 175 – 203.

Jacobsen, S. D., Jiang, F., Mao, Z., Duffy, T. S., Smyth, J. R., Holl, C.M., Frost, D.J. (2008). Effects of hydration on the elastic properties of olivine, Geophysical Research Letters. 35, doi:10.1029/2008GL034398.

Karato, S. (1993). Importance of anelasticity in the interpretation of seismic tomography, Geophysical Research Letters. 20, 1623 – 1626.

Karato, S. (2008). Deformation of Earth Materials: An Introduction to the Rheology of Solid Earth. Cambridge University Press, p. 394.

Kennett, B.L.N., Engdahl, E.R., Buland, R. (1995). Constraints on seismic velocities in the Earth from travel times. Geophysical Journal International. 122, 108-124.

Kern, H. & Richter, A. (1981). Temperature derivatives of compressional and shear wave velocities in crustal and mantle rocks at 6 kbar confining pressure, Journal of Geophysical Research. 49, 47-56.

Kohler, M. D. (1999). Lithospheric deformation beneath the San Gabriel Mountains in the southern California Transverse Range. Journal of Geophysical Research. 104, 15,025 – 15,041.

Kohler, M. D., Magistrale, H., Clayton, R. W. (2003). Mantle heterogeneities and the SCEC reference three-dimensional seismic velocity model version 3. Bulletin of the Seismological Society of America. 93, 757 – 774.

Kosloff, D. (1977). Numerical simulations of tectonic processes in Southern California. Royal Astronomical Society Geophysical Journal, 51, 487–501.

Lee, C.-T. A. (2003). Compositional variation of density and seismic velocities in natural peridotites at STP conditions: Implications for seismic imaging of compositional heterogeneities in the upper mantle, Journal of Geophysical Research. 108, doi:10.1029/2003JB002413.

Li, X., Yuan, X., Kind, R. (2007). The lithosphere-asthenosphere boundary beneath the western United States. Geophysical Journal International. 170, 700-710.

Lin, F-C., Moschetti, M. P., Ritzwoller, M. H., (2008). Surface wave tomography of the western United States from ambient seismic noise: Rayleigh and Love wave phase velocity maps. Geophysical Journal International. 173, 281–298.

Liu, H., Davis, P. M., Gao, S. (1995). SKS splitting beneath southern California, Geophysical Research Letters. 22, 767 – 770.

Marquering, H., Dahlen, F. A., Nolet, G. (1999). Three dimensional sensitivity kernels for finite-frequency traveltimes: The banana-doughnut paradox. Geophysical Journal International. 137, 805 – 815.

Monfort, M. E. & Evans, J. R. (1982). Three-dimensional modeling of the Nevada Test Site and vicinity from P-wave residuals. United States Geological Survey Reports. 82-409, 1-66.

Nataf, H. C. & Ricard, Y. (1996). 3SMAC: An a priori tomographic model of the upper mantle based on geophysical modeling. Physics of the Earth and Planetary Interiors. 95, 101 – 122.

Paige, C. C. & Saunders, M. A. (1982). LSQR: An algorithm for sparse linear equations and sparse least squares, ACM Trans. Math. Soft., 8, 43–71.

Polet, J. and H. Kanamori (1997), Upper mantle shear velocities beneath southern California determined from long-period surface waves, Bull. Seismol. Soc. Am., 87, 200–209.

Polet, J., and H. Kanamori (2002), Anisotropy beneath California: Shear wave splitting measurements using a dense broadband array, Geophys. J. Int., 149, 313 – 327.

Raikes, S. A. (1980). Regional variations in upper mantle structure beneath southern California. Geophysical Journal of the Royal Astronomical Society. 63, 187–216.

Revenaugh, J. (1995). A scattered-wave image of subduction beneath the Transverse Ranges. Science. 268, 1888-1892

Ritsema, J., van Heijst, H.J., Woodhouse, J. Deuss, A. (2009). Long-period body-wave traveltimes through the crust: implication for crustal corrections and seismic tomography. Geophysical Journal International. 179, 1255–1261.

Saleeby, J. (2003). Segmentation of the Laramide Slab - evidence from the southern Sierra Neveda region. Geological Society of America Bulletin. 115, 655–668.

Saltzer, R. L., and Humphreys, E. D. (1997) Upper mantle P wave velocity structure of the eastern Snake River Plain and its relationship to geodynamic models of the region, Journal of Geophysical Research. 102, 11,829 – 11,841.

Savage, M. K. & Silver, P. G. (1993). Mantle deformation and tectonics: Constraints from seismic anisotropy in the western United States. Physics of the Earth and Planetary Interiors. 78, 207–227.

Schmeling, H. (1985). Numerical models on the influence of partial melt on elastic, anelastic, and electrical properties of rocks, part I, Elasticity and anelasticity, Phys. Earth Planet. Int., 41, 34-57.

Schutt, D. L. & Lesher, C. E. (2006). Effects of melt depletion on the density and seismic velocity of garnet and spinel lherzolite, Journal of Geophysical Research. 111, doi:10.1029/2003JB002950.

Sigloch, K., McQuarrie, N., Nolet, G. (2008). Two-stage subduction history under North America inferred from multiple-frequency tomography. Nature Geoscience. 1, 458–462.

Spence, W., (1974) P-wave residual differences and inferences on an upper mantle source for the Silent Canyon volcanic center, southern Great Basin, Nevada, Geophys. J .R. Astron. Soc., 38, 505-523.

Tape, C., Liu, Q., Maggi, A., Tromp, J. (2009). Adjoint tomography of the southern California crust. Science. 325, doi: 10.1126/science.1175298.

Tian, Y., Zhao, D., Teng, J. (2007). Deep structure of southern California, Physics of the Earth and Planetary Interiors. 165, 93 – 113.

Thurber, C., Zhang, H., Brocher, T., Langenheim, V. (2009). Regional three-dimensional seismic velocity model of the crust and uppermost mantle of northern California. Journal of Geophysical Research. 114, doi:10.1029/2008JB005766.

VanDecar, J. C. & Crosson, R. S. (1990). Determination of teleseismic relative phase arrival times using multi-channel cross-correlation and least squares. Bulletin of the Seismological Society of America. 80, 150 – 169.

Yan, Z., & Clayton, R. W. (2007). Regional mapping of the crustal structure in southern California from receiver functions. Journal of Geophysical Research. 112, doi:10.1029/2006JB004622.

Yang, Y. & Forsyth, D.W. (2006). Rayleigh wave phase velocities, small-scale convection, and azimuthal anisotropy beneath southern California. Journal of Geophysical Research. 111, doi:10.1029/2005JB004180.

Yang, Y. & Forsyth, D.W. (2008). Attenuation in the upper mantle beneath Southern California: Physical state of the lithosphere and asthenosphere. Journal of Geophysical Research. 113, doi:10.1029/2007JB005118.

Yang, Y., Ritzwoller, M. H., Lin, F.-C., Moschetti, M. P., Shapiro, N. M. (2008). Structure of the crust and uppermost mantle beneath the western United States revealed by ambient noise and earthquake tomography. Journal of Geophysical Research. 113, doi:10.1029/2008JB005833.

Zandt, G., Gilbert, H., Owens, T. J., Ducea, M., Saleeby, J., Jones, C. H. (2004). Active foundering of a continental arc root beneath the southern Sierra Nevada in California. Nature. 431, 41–46.

Chapter III

Anderson, O.L., Isaak, D., Oda, H. (1992). High-temperature elastic constant data on minerals relevant to geophysics. Reviews of Geophysics. 30, 57-90.

Atwater, T. (1970). Implications of plate tectonics for Cenozoic tectonic evolution of western North America. Geological Society of America Bulletin. 81, 3513–3536.

Bedle, H. & van der Lee, S. (2009). S velocity variations beneath North America, Journal of Geophysical Research. 114, doi:10.1029/2008JB005949.

Bird, P. & Rosenstock, R. W. (1984). Kinematics of present crust and mantle flow in southern California, Geological Society of America Bulletin. 95, 946–957.

Bird, P. (1984). Laramide crustal thickening event in the rocky mountain foreland and great plains. Tectonics. 3, 741–758.

Bird, P. (1979). Continental delamination and the Colorado Plateau. Journal of Geophysical Research. 84, 7561–7571.

Bunge, H.-P. & Grand, S. (2000). Mesozoic plate-motion history below the northeast Pacific Ocean from seismic images of the subducted Farallon slab. Nature. 405, 337–340.

Burchfiel, B.C., Cowen, D.S., Davis, G.A. (1992). Tectonic overview of the Cordilleran orogen in the western U. S, in The Geology of North America: The Cordilleran Orogen: Conterminous U.S. (eds Burchfiel, B. C., Lipman, P., Zoback, M. L.) Geological Society of America, Boulder, Cololorado, G-3, 407–479.

Burdick, S., van der Hilst, R.D., Vernon, F.L., Martynov, V., Cox, T., Eakins, J., Astiz, L., Pavlis, G.L. (2009). Model Update December 2008: Upper Mantle Heterogeneity beneath North America from P-wave Travel Time Tomography with Global and USArray Transportable Array Data. Seismological Research Letters. 80, 638 – 645.

Christiansen, R.L. & Yeats, R.S. (1992). Post-Laramide geology of the Cordilleran region: The Cordilleran Orogen, Conterminous U.S. The Geology of North America, 3, 261–406.

Chulick, G. S. & Mooney, W. D. (2002). Seismic structure of the crust and uppermost mantle of North America and adjacent oceanic basins: A synthesis. Bulletin of the Seismological Society of America. 92, 2478-2492.

Coney, P. J. & Reynolds, S. J. (1977). Flattening of the Farallon slab. Nature. 270, 403–406.

Coney, P. J. & Harms, T. A. (1984). Cordilleran metamorphic core complexes: Cenozoic extensional relics of Mesozoic compression. Geology, 12, 550–554.

Dahlen, F.A., Hung, S.-H., Nolet, G. (2000). Frechet kernels for finite-frequency traveltimes, I. Theory, Geophysical Journal International. 141, 157–174.

Dalton, C.A., Ekstrom, G., Dziewonski, A.M., 2008. The global attenuation structure of the upper mantle. Journal of Geophysical Research. 113, B09303, doi:10.1029/2007JB005429.

DeCelles, P.G. (2004). Late Jurassic to Eocene evolution of the Cordilleran thrust belt and foreland basin system, western U.S.A. American Journal of Science. 304, 105-168.

Dickinson, W. R. & Snyder, W. S. (1979). Geometry of subducted slabs related to the San Andreas transform. Journal of Geology. 87, 609–627.

Ducea, M. & Saleeby, J. (1998). A case for delamination of the deep batholithic crust beneath the Sierra Nevada, California. International Geology Reviews. 40, 78 – 93.

Engebretsen, D. C., Cox, A., Gordon, R. G. (1985). Relative motions between oceanic and continental plates in the Pacific Basin. Geological Society of America Special Paper. 206, 560–569.

Gao, W. (2004). Upper mantle convection beneath the central Rio Grande rift imaged by P and S wave tomography. Journal of Geophysical Research. 109, doi:10.1029/2003JB002743.

Gaschnig, R. M., Vervoort, J. D., Lewis, R. S., McClelland, W. C. (2009). Migrating magmatism in the northern US Cordillera: in situ U–Pb geochronology of the Idaho batholith. Contributions to Mineralogy and Petrology. 111, doi:10.1007/s00410-009-0459-5.

Goes, S., Govers, R., Vacher, P. (2000). Shallow mantle temperatures under Europe from P and S wave tomography, Journal of Geophysical Research. 105, 11,153 – 11,170.

Goes, S. & van der Lee, S. (2002). Thermal structure of the North American uppermost mantle inferred from seismic tomography. Journal of Geophysical Research. 107, doi:10.1029/2000JB000049.

Golombek, M. P., McGill, G. E., Brown, L. (1983). Tectonic and geologic evolution of the Española Basin, Rio Grande rift: structure, rate of extension, and relation to the state of stress in the Western US. Tectonophysics. 94, 483–507.

Grand, S. P. (1994). Mantle shear structure beneath the Americas and surrounding oceans. Journal of Geophysical Research. 99, 11,591–11,621.

Gripp, A. E. & Gordon, R. G. (2002). Young tracks of hotspots and current plate velocities. Geophysical Journal International. 150, 321–361.

Hales, T. C., Abt, D.L., Humphreys, E. D., Roering, J. J. (2005). A lithospheric instability origin for Columbia River flood basalts and Wallowa Mountains uplift in northeast Oregon. Nature. 438, 842–845.

Hammond, W. C. & Humphreys, E. D. (2000). Upper mantle seismic wave velocity: Effects of realistic partial melt geometries. Journal of Geophysical Research. 105, 975–986.

Hammond, W. C. & Toomey, D. R. (2003). Seismic velocity anisotropy and heterogeneity beneath the Mantle Electromagnetic and Tomography Experiment (MELT) region of the East Pacific Rise from analysis of P and S body waves. Journal of Geophysical Research. 108, doi:10.1029/2002JB001789.

Heller, P. L., Dueker, K., McMillan, M. (2003). Post-Paleozoic alluvial gravel transport as evidence of continental tilting in the Cordilleran, United States. Geological Society of America Bulletin. 115, 1122–1132.

Hirschmann, M. M. (2006). Water, melting, and the deep earth H2O cycle. Annual Reviews of Earth and Planetary Science. 34, 629 – 653.

Humphreys, E. D. & Hager, B. H. (1990). A kinematic model for the late Cenozoic development of southern California crust and upper mantle. Journal of Geophysical Research. 95, 19,747–19,762.

Humphreys, E. D. & Dueker, K. (1994). Western U.S. upper mantle structure. Journal of Geophysical Research. 99, 9615–9634.

Humphreys, E. D. (1995). Post-Laramide removal of the Farallon slab, western United States. Geology. 23, 987–990.

Humphreys, E. D. (2009). Cenozoic slab windows beneath the western U.S. Arizona Geological Society Digest. 22, 389–396.

Humphreys, E. D. (2003). How Laramide-age hydration of North American lithosphere by the Farallon slab controlled subsequent activity in the western U. S. International Geology Reviews. 45, 575–595.

Jacobsen, S. D. (2008). Effects of hydration on the elastic properties of olivine. Geophysical Research Letters. 35, doi:10.1029/2008GL034398.

Karato, S. (1993). Importance of anelasticity in the interpretation of seismic tomography. Geophysical Research Letters. 20, 1623 – 1626.

Karlstrom, K. E, Crow, R., Crossey, L. J., Coblentz, D., Van Wijk, J. W. (2008). Model for tectonically driven incision of the younger than 6 Ma Grand Canyon. Geology. 36, 835–838.

Kennett, B.L.N., Engdahl, E.R., Buland, R. (1995). Constraints on seismic velocities in the Earth from travel times. Geophysical Journal International. 122, 108-124.

Kern, H. & Richter, A. (1981). Temperature derivatives of compressional and shear wave velocities in crustal and mantle rocks at 6 kbar confining pressure. Journal of Geophysical Research. 49, 47-56.

Lebedev, S. & van der Hilst, R. (2008). Global upper mantle tomography with the automated inversion of surface and S-waveforms. Geophysical Journal International. 173, 505-518.

Lee, C.-T.A. (2003). Compositional variation of density and seismic velocities in natural peridotites at STP conditions: Implications for seismic imaging of compositional heterogeneities in the upper mantle. Journal of Geophysical Research. 108, doi:10.1029/2003JB002413.

Li, X., Yuan, X., Kind, R. (2007). The lithosphere-asthenosphere boundary beneath the western United States, Geophysical Journal International. 170, 700-710.

Lin, F-C., Moschetti, M. P., Ritzwoller, M. H. (2008). Surface wave tomography of the western United States from ambient seismic noise: Rayleigh and Love wave phase velocity maps. Geophysical Journal International. 173, 281–298.

Lithgow-Bertelloni, C. & Richards, M. A. (1998). The dynamics of Cenozoic and Mesozoic plate motions. Reviews of Geophysics. 36, 27–78.

Livaccari, R.F., Burke, K., Sengor, A.M.C. (1981). Was the Laramide orogeny related to subduction of an oceanic plateau? Nature. 289, 276–278.

Lowry, A.R., Ribe, N.M., Smith, R.B., 2000. Dynamic elevation of the Cordillera, western United States. Journal of Geophysical Research. 105(B10), 23,371–23,390.

Madsen, J.K., Thorkelson, D. J., Friedman, R. M., Marshall, D. D. (2006). Cenozoic to Recent plate configurations in the Pacific Basin: Ridge subduction and slab window magmatism in western North America. Geosphere. 2, 11–34.

Monfort, M. E. & Evans, J. R. (1982). Three-dimensional modeling of the Nevada Test Site and vicinity from P-wave residuals. United States Geological Survey Reports. 82-409, 1-66.

Muller, R. D., Sdrolias, M., Gaina, G., Roest, W. R. (2008). Age, spreading rates, and spreading asymmetry of the world's ocean crust. Geochemistry Geophysics Geosystems. 9, doi:10.1029/2007GC001743.

Piromallo, C., Becker, T. W., Funiciello, F., Faccenna, C. (2006). Three-dimensional instantaneous mantle flow induced by subduction. Geophysical Research Letters. 33, doi: 10.1029/2005GL025390.

Pollitz, F. F. & Snoke, J. A. (2010). Rayleigh-wave phase-velocity maps and three-dimensional shear velocity structure of the western US from local non-plane surface wave tomography. Geophysical Journal International. 180, 1153-1169.

Reiners, P. W. (2002). Late Miocene exhumation and uplift of the Washington Cascades, Geology. 30, 767-770.

Riihimaki, C. A., Anderson, R. S., Safran, E. B., (2007). Impact of rock uplift on rates of late Cenozoic Rocky Mountain river incision. Journal of Geophysical Research. 112, doi:10.1029/2006JF000557.

Ritsema, J., van Heijst, H. J., Woodhouse, J., Deuss, A. (2009). Long-period body-wave traveltimes through the crust: implication for crustal corrections and seismic tomography. Geophysical Journal International. 179, 1255–1261.

Romanowicz, B. (1979). Seismic structure of the upper mantle beneath the United States by three dimensional inversion of body wave arrival times. Geophysical Journal of the Royal Astronomical Society. 57, 479–506.

Roth, J. B., Fouch, M. J., James, D. E., Carlson, R. W. (2008). Three-dimensional seismic velocity structure of the northwestern United States. Geophysical Research Letters. 35, L15304.

Roy, M., Jordan, T. H., Pederson, J. (2009). Colorado Plateau magmatism and uplift by warming of heterogeneous lithosphere. Nature. 459, 978-982.

Saleeby, J. (2003). Segmentation of the Laramide Slab - evidence from the southern Sierra Neveda region. Geological Society of America Bulletin. 115, 655–668.

Schmandt, B. & Humphreys, E. D. (2010). Seismic heterogeneity and small-scale convection in the southern California upper mantle. Geochemistry Geophysics. Geosystems. 11, 2010GC003042RR.

Schutt, D. L. & Dueker, K. (2008). Temperature of the plume layer beneath the Yellowstone hotspot. Geology. 36, 623–626.

Sigloch, K., McQuarrie, N., Nolet, G. (2008). Two-stage subduction history under North America inferred from multiple-frequency tomography. Nature Geoscience. 1, 458–462.

Sine, C. R. (2008). Mantle structure beneath the western edge of the Colorado Plateau. Geophysical Research Letters. 35, doi:10.1029/2008GL033391.

Smith, R. B. (2009). Geodynamics of the Yellowstone hotspot and mantle plume: Seismic and GPS imaging, kinematics, and mantle flow. Journal of Volcanology and Geothermal Research. 188, doi:10.1016/j.jvolgeores.2009.08.020.

Song, T.-R.A. & Helmberger, D. V. (2007). P and S waveform modeling of continental sub-lithospheric detachment at the eastern edge of the Rio Grande Rift. Journal of Geophysical Research. 112, doi:10.1029/2007JB004942.

Spencer, J. E. (1996). Uplift of the Colorado Plateau due to lithosphere attenuation during Laramide low-angle subduction. Journal of Geophysical Research. 101, 13,595–13,609.

Stachnik, J. C., Dueker, K., Schutt, D. L., Yuan, H. (2008). Imaging Yellowstone plume-lithosphere interactions from inversion of ballistic and diffusive Rayleigh wave dispersion and crustal thickness data. Geochemistry Geophysics Geosystems. 9, doi:10.1029/2008GC001992.

Stock, J. & Molnar, P. (1988). Uncertainties and implications of the Late Cretaceous and Tertiary position of North America relative to the Farallon, Kula, and Pacific plates. Tectonics. 7, 1339–1384.

Tape, C., Liu, Q., Maggi, A., Tromp, J. (2009). Adjoint tomography of the southern California crust. Science. 325, doi: 10.1126/science.1175298.

Thurber, C., Zhang, H., Brocher, T., Langenheim, V. (2009). Regional three-dimensional seismic velocity model of the crust and uppermost mantle of northern California. Journal of Geophysical Research. 114, doi:10.1029/2008JB005766.

Tian, Y., Sigloch, K., Nolet, G. (2009). Multiple-frequency SH-wave tomography of the western US upper mantle. Geophysical Journal International. 178, doi:10.1111/j.1365-246X.2009.04225.x.

VanDecar, J. C. & Crosson, R. S. (1990). Determination of teleseismic relative phase arrival times using multi-channel cross-correlation and least squares. Bulletin of the Seismological Society of America. 80, 150 – 169.

van der Lee, S. & Nolet, G. (1997). Seismic image of the subducted trailing fragments of the Farallon plate. Nature. 386, 266 - 269.

West, J. D., Fouch, M. J., Roth, J. B., Elkins-Tanton, L. T. (2009). Vertical mantle flow associated with a lithospheric drip beneath the Great Basin. Nature Geoscience. 2, 439-444.

Yang, Y. & Forsyth, D. W. (2008). Attenuation in the upper mantle beneath Southern California: Physical state of the lithosphere and asthenosphere. Journal of Geophysical Research. 113, doi:10.1029/2007JB005118.

Yang, Y., Ritzwoller, M. H., Lin, F.-C., Moschetti, M. P., Shapiro, N. M. (2008). Structure of the crust and uppermost mantle beneath the western United States revealed by ambient noise and earthquake tomography. Journal of Geophysical Research. 113, doi:10.1029/2008JB005833.

Yuan, H. & Dueker, K. (2005). Teleseismic P-wave Tomogram of the Yellowstone Plume. Geophysical Research Letters. 32. doi:10.1029/ 2004GL022056.

Zandt, G., Gilbert, H., Owens, T. J., Ducea, M., Saleeby, J., Jones, C. H. (2004). Active foundering of a continental arc root beneath the southern Sierra Nevada in California. Nature. 431, 41–46.

Zandt, G. & Humphreys, E. D. (2008). Toroidal through the western U.S. slab window. Geology. 36, 295-298.

Chapter IV

Bird, P. (1979). Continental delamination and the Colorado Plateau, Journal of Geophysical Research. 84, 7561-7571.

Breitsprecher, K, Thorkelson, D. J., Groome, W. G., Dostal, J. (2003). Geochemical confirmation of the Kula-Farallon slab window beneath the Pacific Northwest in Eocene time. Geology. 31, 351–354.

Burdick, S., van der Hilst, R.D., Vernon, F.L., Martynov, V., Cox, T., Eakins, J., Astiz, L., Pavlis, G.L. (2009). Model Update December 2008: Upper Mantle Heterogeneity beneath North America from P-wave Travel Time Tomography with Global and USArray Transportable Array Data. Seismological Research Letters. 80, 638 – 645.

Christiansen, R.L. & Yeats, R.S. (1992). Post-Laramide geology of the Cordilleran region: The Cordilleran Orogen, Conterminous U.S. The Geology of North America, 3, 261–406.

Cloos, M. (1993). Lithospheric buoyancy and collisional orogenesis: Subduction of oceanic plateaus, continental margins, island arcs, spreading ridges and seamounts, Geological Society of America Bulletin. 105, 715–773.

Coney, P. J., & Reynolds, S. J. (1977). Flattening of the Farallon slab. Nature. 270, 403–406.

Coney, P.J. & Harms, T.A., 1984, Cordilleran metamorphic core complexes: Cenozoic extensional relics of Mesozoic compression. Geology. 12, 550–554.

Dalton, C. A., Ekstrom, G., Dziewonski, A. M. (2008). The global attenuation structure of the upper mantle. Journal of Geophysical Research. 113, doi:10.1029/2007JB005429.

Dickinson, W. R. (2006). Geotectonic evolution of Great Basin: Geosphere. 2, 353-368.

Eagar, K. C., Fouch, M. J., James, D.E. (2010). Receiver function imaging of upper mantle complexity beneath the Pacific Northwest, United States, Earth and Planetary Science Letters. 297, doi:10.1016/j.epsl.2010.06.015.

Feeley, T.C. (2003). Origin and Tectonic Implications of Across-Strike Geochemical Variations in the Eocene Absaroka Volcanic Province, United States. Journal of Geology. 111, 329–346.

Foster, D. A., Doughty, P. T., Kalakay, T. J., Fanning, C. M., Coyner, S., Grice, W. C., Vogl, J. (2007). Kinematics and timing of exhumation of metamorphic core complexes along the Lewis and Clark fault zone, northern Rocky Mountains, USA. Geological Society of America Special Publication, 434, 207–232.

Gaschnig, R. M., Vervoot, J. D., Lewis, R. S., McClelland, W. C. (2009). Migrating magmatism in the northern US Cordillera: in situ U-Pb geochronology of the Idaho Batholith: Contributions to Mineralogy and Petrology. 117, doi:10.1007/s00410-009-0459-5.

Gehrels, G. (2009). U-Th-Pb geochronology of the Coast Mountains batholith in north-coastal British Columbia: Constraints on age and tectonic evolution. Geological Society of America Bulletin. 121, 1341–1361.

Gilbert, H. & Flesch, L. M. (2009). Using Earthscope data to separate the influences of inherited lithospheric structures and more recent tectonics in driving the dynamics of the western United States. Eos Transactions of the American Geoiphysical Union, 90, U52A-05.

Giorgis, S., Tikoff, B., McClelland, W. (2005). Missing Idaho arc: Transpressional modification of the $^{87}Sr/^{86}Sr$ transition on the western edge of the Idaho batholith. Geology. 33, 469-472.

Gurnis, M. (1992). Rapid continental subsidence following the initiation and evolution of subduction: Nature, 255, 1556–1558.

Hales, T. C., Abt, D., Humphreys, E., Roering, J. (2005). A lithospheric instability origin for Columbia River flood basalts and Wallowa Mountains uplift in northeast Oregon. Nature. 438, 842–845.

Humphreys, E. D. (1995). Post-Laramide removal of the Farallon slab, western United States, Geology, 23, 987–990.

Humphreys, E., Dueker, K. G., Schutt, D. L., Smith, R. B. (2000). Beneath Yellowstone; evaluating plume and nonplume models using teleseismic images of the upper mantle. Geological Society of America Today, 10, 1-7.

Karato S. (1993). Importance of anelasticity in the interpretation of seismic tomography. Geophysical Research Letters, 20,1623-1626.

Karato, S. (2003). Mapping water content in the upper mantle: Inside the Subduction Factory. AGU Monograph, 138, 135–152.

Kustowski, B., Ekstrom, G., & Dziewonski, A. D., 2008, Anisotropic shear-wave velocity structure of the Earth's mantle: A global model, Journal of Geophysical Research: v. 113, doi:10.1029/2007JB005169.

Long, M. D., Gao, H., Klaus, A., Wagner, L. S., Fouch, M. J., James, D. E., Humphreys, E. D. (2009). Shear wave splitting and the pattern of mantle flow beneath eastern Oregon: Earth and Planetary Science Letters, 288, 359-369.

Madsen, J. K., Thorkelson, D. J., Friedman, R. M., Marshall, D. D. (2006). Cenozoic to Recent plate configurations in the Pacific Basin: Ridge subduction and slab window magmatism in western North America: Geosphere. 2, 11–34.

Muller, R. D., Sdrolias, M., Gaina, G., Roest, W. R. (2008). Age, spreading rates, and spreading asymmetry of the world's ocean crust, Geochemistry Geophysics Geosystems. 9, doi:10.1029/2007GC001743.

Retallack, G. J., Bestland, E. A., Fremd, T. (2000). Eocene and Oligocene paleosols of central Oregon. Geological Society of America Special Publication. 344, doi: 10.1130/0-81372344-2.1.

Riddihough, R., Finn, C., Couch, R. (1986). Klamath-Blue Mountain lineament, Oregon. Geology. 14, 528–531.

Roth, J. B., Fouch, M. J., James, D. E., Carlson, R. W. (2008). Three-dimensional seismic velocity structure of the northwestern United States. Geophysical Research Letters, 35, L15304.

Schmandt, B. & Humphreys, E. (2010a). Complex subduction and small-scale convection revealed by body-wave tomography of the western United States upper mantle. Earth and Planetary Science Letters. 297, doi:10.1016/j.epsl.2010.06.047

Schmandt, B. & Humphreys, E. (2010b). Seismic heterogeneity and small-scale convection in the southern California upper mantle. Geochemistry Geophysics Geosystems. 11, doi:10.1029/2010GC003042.

Sigloch, K., McQuarrie, N., Nolet, G. (2008). Two-stage subduction history under North America inferred from multiple-frequency tomography. Nature Geoscience. 1, 458–462.

Tian, Y., Sigloch, K., Nolet, G. (2009). Multiple-frequency SH-wave tomography of the western U.S. upper mantle. Geophysical Journal International. 178, 1384–1402.

van der Pluijm, B.A., Vrolijk, P.J., Pevear, D.R., Hall, C.M., Solum, J.G. (2006). Fault dating in the Canadian Rocky Mountains: Evidence for late Cretaceous and early Eocene orogenic pulses. Geology. 34, 837–840.

van Keken, P. E., Keifer, B., Peacock, S. M. (2002). High-resolution models of subduction zones: Implications for mineral dehydration reactions and transport of water into the deep mantle. Geochemistry Geophysics Geosystems. 3, doi:10.1029/2001GC000256.

Walker, J. D., Bowers, T. D., Glazner, A. F., Farmer, A. L., and Carlson, R. W. (2004). Creation of a North American volcanic and plutonic rock database (NAVDAT). Geological Society of America Abstracts with Programs, 36, 9.

Wang, Y., Forsyth, D. W., Savage, B. (2009). Convective upwelling in the mantle beneath the Gulf of California. Nature. 462, doi:10.1038/nature08552.

Wells, R. E., Engebretson, D. C., Snavely, P. D., Coe, R. S. (1984). Cenozoic plate motions and the volcano-tectonic evolution of western Oregon and Washington: Tectonics, v. 3, p. 275–294.

Xue, M. & Allen, R.M. (2010). Mantle structure beneath the western United States and its implications for convection processes. Journal of Geophysical Research. 115, doi:10.1029/2008JB006079.

Yang, Y., Ritzwoller, M. H., Lin, F.-C., Moschetti, M. P., Shapiro, N. M. (2008). Structure of the crust and uppermost mantle beneath the western United States revealed by ambient noise and earthquake tomography. Journal of Geophysical Research. 113, doi:10.1029/2008JB005833.

Zhang, X., Paulssen, H., Lebedev, S., Meier, T. (2009). 3D shear velocity structure beneath the Gulf of California from Rayleigh wave dispersion. Earth and Planetary Science Letters. 279, 255–262.